

Infrared spectra of complex organic molecules in astronomically relevant ice mixtures

IV. Methylamine[★]

M. G. Rachid¹ , N. Brunken¹ , D. de Boe¹, G. Fedoseev^{1,2} , A. C. A. Boogert³, and H. Linnartz¹ 

¹ Laboratory for Astrophysics, Leiden Observatory, Leiden University, PO Box 9513, NL2300 RA Leiden, The Netherlands
e-mail: rachid@strw.leidenuniv.nl

² Research Laboratory for Astrochemistry, Ural Federal University, Kuibysheva St. 48, 620026 Ekaterinenburg, Russia

³ Institute for Astronomy, University of Hawai'i at Mānoa, 2680 Woodlawn Drive, Honolulu, HI 96822, USA

Received 10 March 2021 / Accepted 12 June 2021

ABSTRACT

Context. In the near future, high spatial and spectral infrared (IR) data of star-forming regions obtained by the *James Webb* Space Telescope may reveal new solid-state features of various species, including more intriguing classes of chemical compounds. The identification of complex organic molecules (COMs) in the upcoming data will only be possible when laboratory IR ice spectra of these species under astronomically relevant conditions are available for comparison. For this purpose, systematic series of laboratory measurements are performed, providing high-resolution IR spectra of COMs. Here, spectra of pure methylamine (CH_3NH_2) and methylamine-containing ices are discussed.

Aims. The work is aimed at characterizing the mid-IR ($500\text{--}4000\text{ cm}^{-1}$, $20\text{--}2.5\text{ }\mu\text{m}$) spectra of methylamine in pure and mixed ices to provide accurate spectroscopic data of vibrational bands that are most suited to trace this species in interstellar ices.

Methods. Fourier transform infrared spectroscopy is used to record spectra of CH_3NH_2 in the pure form and mixed with H_2O , CH_4 , and NH_3 , for temperatures ranging from 15 to 160 K. The IR spectra in combination with HeNe laser (632.8 nm) interference data of pure CH_3NH_2 ice was used to derive the IR band strengths of methylamine in pure and mixed ices.

Results. The refractive index of amorphous methylamine ice at 15 K was determined as being 1.30 ± 0.01 . Accurate spectroscopic information and band strength values are systematically presented for a large set of methylamine-containing ices and different temperatures. Selected bands are characterized and their use as methylamine tracers is discussed. The selected bands include the following: the CH_3 antisymmetric stretch band at 2881.3 cm^{-1} ($3.471\text{ }\mu\text{m}$), the CH_3 symmetric stretch band at 2791.9 cm^{-1} ($3.582\text{ }\mu\text{m}$), the CH_3 antisymmetric deformation bands, at 1455.0 and 1478.6 cm^{-1} (6.873 and $6.761\text{ }\mu\text{m}$), the CH_3 symmetric deformation band at 1420.3 cm^{-1} ($7.042\text{ }\mu\text{m}$), and the CH_3 rock at 1159.2 cm^{-1} ($8.621\text{ }\mu\text{m}$). Using the laboratory data recorded in this work and ground-based spectra of ices toward YSOs (Young Stellar Objects), upper-limits for the methylamine ice abundances are derived. In some of these YSOs, the methylamine abundance is less than 4% relative to H_2O .

Key words. astrochemistry – molecular data – methods: laboratory: molecular – methods: laboratory: solid state – ISM: molecules – techniques: spectroscopic

1. Introduction

Amino acids are key molecules to life on Earth. Whereas such species have been found in meteorites, already more than half a century ago (Kvenvolden et al. 1970), the simplest amino acid, glycine ($\text{NH}_2\text{CH}_2\text{COOH}$) still has not been unambiguously detected in the interstellar medium (ISM). Its formation pathways in the gas phase and in the solid state have been a matter of ongoing debate (Elsila et al. 2007). A direct consequence of this has been that several molecules, regarded as potential glycine precursors, have become a target in new surveys with the ultimate goal being point out sources that may host glycine at a detectable level. Recent examples include the search for amino acetonitrile ($\text{NH}_2\text{CH}_2\text{CN}$) by Belloche et al.

(2008), methanimine (CH_2NH) by Suzuki et al. (2016), hydroxylamine (NH_2OH) by McGuire et al. (2015), and methylamine (CH_3NH_2) by Ohishi et al. (2019). Such species are expected to have a solid state origin and in this respect methylamine is of special interest, as in recent laboratory work by Ioppolo et al. (2021), it was shown to form nonthermally, under dark cloud conditions (i.e., without impacting UV photons) in a chain of solid-state reactions that also leads to glycine. Fully in line with these experiments was the recent detection of both species in the comet 67P/Churyumov-Gerasimenko (Altwegg et al. 2016), whose composition is considered to reflect the chemical material of the prestellar core from which our Solar System originated (Mumma & Charnley 2011). For these reasons, we aim in this study to provide high resolution solid-state infrared (IR) spectra of methylamine ice, both pure and embedded in astronomically relevant ice matrices. These data are currently lacking and these allow one to search for frozen methylamine in the ISM, also adding further options to optimize the search for interstellar glycine.

* Tables from Appendices B and C are only available at the CDS via anonymous ftp to cdsarc.u-strasbg.fr (130.79.128.5) or via <http://cdsarc.u-strasbg.fr/viz-bin/cat/J/A+A/653/A116>

The first CH_3NH_2 detection dates back to 1974 when it was identified toward Sgr B2 and Orion A (Kaifu et al. 1974; Fourikis et al. 1974). Since then, methylamine has also been detected in other high mass star-forming regions (Bøgelund et al. 2019; Ohishi et al. 2019) and in our own Solar System, in the material from the comets Wild 2 and 67P/Churyumov-Gerasimenko (Glavin et al. 2008; Goesmann et al. 2015; Altwegg et al. 2016). Also recently, Ohishi et al. (2019) used the radio telescope Nobeyama to search for methylamine toward several hot molecular cores, which resulted in the detection of a new CH_3NH_2 source, G10.47+0.03, the richest methylamine source up to date.

Several interstellar reaction pathways toward methylamine have been proposed, both in the gas phase and in the solid state. In the gas phase, CH_3NH_2 can be formed by the reaction of a methyl radical cation with ammonia, followed by dissociative recombination (Leung et al. 1984; Herbst 1985; Maeda & Ohno 2006). The photolysis of gaseous mixtures containing CH_4 , NH_3 , and H_2O is also effective to form methylamine (Gardner & McNesby 1980; Ogura et al. 1988, 1989). Gardner & McNesby (1980) demonstrated that the condensation of a gaseous $\text{CH}_4:\text{NH}_3:\text{H}_2\text{O}$ mixture followed by UV irradiation provided a solid-state channel resulting in the formation of methylamine. This solid-phase reaction has been included in a gas-grain chemical network by Garrod et al. (2008), who pointed out that the CH_3 and NH_2 radicals can be formed on the ice grains by UV or cosmic rays (CR), indicating that methylamine can be formed at very early stages inside dark molecular clouds. Additionally, Theulé et al. (2011) demonstrated that the hydrogenation of HCN can lead to the formation of CH_3NH_2 at 15 K. The mechanism for this synthesis involves multiple hydrogenation steps, possibly passing through the intermediate methanimine (CH_2NH). The electron irradiation of $\text{CH}_4:\text{NH}_3$ ices was also shown to form methylamine in the solid phase (Kim & Kaiser 2011; Förstel et al. 2017).

Similar to NH_3 , methylamine can act as an electron donor at low temperatures, forming salts and complexes in the solid state (Bossa et al. 2009, 2010; Kayi et al. 2011; Noble et al. 2014). Bossa et al. (2009) showed that CH_3NH_2 thermally reacts with CO_2 at temperatures between 50 and 70 K, forming methylammonium methylcarbamate $[(\text{CH}_3\text{NH}_3^+)(\text{CH}_3\text{NHCOO}^-)]$, which can be converted to glycine (Gly) under UV photolysis:



More recently, Mahjoub & Hodyss (2018) also showed that methylamine can thermally react with carbonyl sulfide (OCS) in the solid phase to form the methylammonium methylthiocarbamate salt $[(\text{CH}_3\text{NH}_3^+)(\text{CH}_3\text{NHOC}^-)]$. The salt formation by nitrogen-bearing molecules is of great importance since these reactions can result in an increase of their sublimation temperatures, “locking” these species on ices at relatively high temperatures (Bossa et al. 2009).

Many solid-state routes have been shown to result in CH_3NH_2 formation, and given its relevance as an amino acid precursor, it is essential to study this species’ solid-state spectral features. The mid-IR spectrum of solid CH_3NH_2 has been reported in the literature in pure form and isolated in Ar and Kr matrices (Durig et al. 1968; Wolff 1970; Durig & Zheng 2001). The infrared spectra of some CH_3NH_2 -containing ices are reported in previous works (Bossa et al. 2009; Kayi et al. 2011; Vinogradoff et al. 2013), but a systematic study of the mid-infrared spectrum of methylamine recorded for different astrochemical relevant

conditions is still lacking. To address this sparsity of laboratory data, we present the spectra of methylamine in mixtures containing H_2O , CH_4 , and NH_3 for temperatures ranging from 15 up to 160 K. The molecules used in the studied samples are amongst the most abundant detected species in water-rich interstellar ices (Boogert et al. 2015), moreover CH_4 and NH_3 are expected to be solid-state precursors of methylamine (Kim & Kaiser 2011; Förstel et al. 2017; Ioppolo et al. 2021). The chosen ice compositions aim to simulate the conditions in which methylamine is expected to be present in icy dust grains. This permits tracking changes in the spectral appearance of vibrational modes with alterations in the ice morphology. The IR bands that carry the highest potential as tracers of methylamine in interstellar ices are selected for in-depth spectral surveys. These IR features are characterized in terms of peak position and full width at half maximum (FWHM), and their relative band strengths in ices at 15 K are derived.

The data presented here are part of a series of laboratory experiments supporting upcoming observations with the *James Webb Space Telescope* (JWST) within the framework of “ICE AGE”, a JWST ERS program. The Mid-InfraRed instrument (MIRI) on board JWST will provide infrared spectra of star-forming regions between 5 and 28.5 μm . These data allow one to identify new species in ices and increasing our insight about the morphology and thermal history of ices in space. The secure assignment of the solid-state features in JWST spectra will only be possible when combined with laboratory spectra of ices recorded for similar astrophysical conditions. The data presented here is publicly available¹, and spectra of ices recorded for intermediate temperatures can be supplied upon request.

This manuscript is organized in the following way: Sect. 2 provides information on the measurements and applied methodology, including details on the band strength measurements. Section 3 presents the overall IR spectra and focuses on bands that might be useful for astronomical identification of solid methylamine. This is illustrated in Sect. 4 discussing the potential of these IR features for tracing solid methylamine. The final section summarizes this work with a conclusion. The essential data resulting from this work are available from the Appendices. Appendix A presents the IR spectra of pure and mixed methylamine ices as well as graphical representations of the relative band strengths and peak position versus FWHM for the selected bands. Appendix B provides data on the peak position and FWHM for these methylamine bands in different ice samples. Appendix C provides the integrated absorbance of the analyzed methylamine bands.

2. Methodology

The experiments have been performed with two setups. The infrared spectra were recorded with our HV (High Vacuum) setup. Details of this system and methodology are available from Terwisscha van Scheltinga et al. (2018) and Rachid et al. (2020). Over the last year, this setup has been fully upgraded, replacing the high vacuum by an UHV system. The new IRASIS (InfraRed Absorption Setup for Ice Spectroscopy) system allows to record IR ice spectra and simultaneously to perform laser interference measurements to determine ice thickness. For both setups, all relevant experimental information is provided below.

The infrared measurements of the pure CH_3NH_2 ice and CH_3NH_2 mixed in H_2O , NH_3 , and CH_4 ices are conducted with

¹ <https://icedb.strw.leidenuniv.nl/>

the HV setup in a high vacuum stainless steel chamber that operates with a base pressure of $\sim 3 \times 10^{-7}$ mbar. Inside the chamber, an IR transparent zinc selenide (ZnSe) window is mounted on a copper holder connected to a cold finger and is maintained at 15 K by a closed-cycle He cryostat. Pure or premixed gases, contained in a 2 L glass bulb with a total pressure of 20 mbar, are admitted into the chamber through a precalibrated needle valve and background deposited onto the substrate. The ices are grown for approximately 30 min, which results in ices with total column densities of $1\text{--}3 \times 10^{18}$ molecules cm^{-2} . After deposition, the ice is heated at a rate of 25 K h^{-1} until its complete sublimation. During both the deposition and ice heating, mid-IR spectra ($20\text{--}2.5 \text{ }\mu\text{m}$, $500\text{--}4000 \text{ cm}^{-1}$ at resolution 0.5 cm^{-1} , averaged over 256 scans) are acquired continuously using a Varian 670 Fourier transform spectrometer. During a single spectrum acquisition period, the ice is heated by roughly 3.5 K. Apart from temperatures close to crystallization or the thermal desorption point, this barely affects band profiles.

The gas mixtures are prepared in a separate mixing system by the sequential addition of gases or vapor components in a 2 L glass bulb. This is done by adding a certain gas/vapor into the glass balloon and freezing this component by immersing the balloon in a liquid nitrogen bath. The freezing of a component gas ensures that this component cannot diffuse into the volume from which the upcoming component is added. For all measurements, the bulb is prepared by filling it with a total pressure of 20 mbar. For gaseous mixtures, each component's partial pressure in the mixture corresponds to the desired ratio in the ice sample. The estimated error in each component ratio following this method is $\leq 10\%$. The gases and liquids used for preparing the gaseous mixtures are CH_3NH_2 (Sigma Aldrich, anhydrous $\geq 99.99\%$), H_2O (Milli-Q, Type I), CH_4 (Linde Gas 99.995%), and NH_3 (Sigma Aldrich, anhydrous $\geq 99.99\%$).

The measurements of the methylamine band strengths are performed in the new experimental setup, IRASIS. This setup allows for the simultaneous acquisition of infrared spectra and laser interference measurements of the growing ice. Figure 1 shows a schematic picture of IRASIS. The central stainless chamber is kept at ultra-high vacuum (base pressure $\sim 2 \times 10^{-9}$ mbar) by a turbomolecular pump (Turbovac i350) pre-pumped by a rotary vane pump supplied with an oil filter. Compared to the previous HV setup, the measurements performed on IRASIS are less sensitive to water ice growth caused by background gas deposition. In the center of the chamber, a Germanium (Ge) substrate is attached to the tip of the cryostat's cold finger. The cryostat head system is mounted onto a rotatable platform, which allows the sample's rotation by 360° . The ice is deposited on both sides of the substrate, and the thickness on each side is monitored during growth by using a HeNe laser ($\lambda = 632.8 \text{ nm}$) interference pattern. The ice thickness (d) is related to the number of interference fringes (m) by (Tempelmeyer & Mills Jr 1968):

$$d = \frac{m\lambda}{2\sqrt{n^2 - \sin^2 \theta}}, \quad (1)$$

where λ is the wavelength of the laser, n is the refractive index of the ice, and θ is the incident angle of the laser beam. Since the Ge substrate is opaque for the light at 632.8 nm , each laser beam probes only the ice growing on one side of the substrate. The reflected light beams are measured by two separate photodetectors (Thorlabs PDA36A2) connected to a data acquisition card (National Instruments) that is controlled using a LabView program, which enables the simultaneous data acquisition from

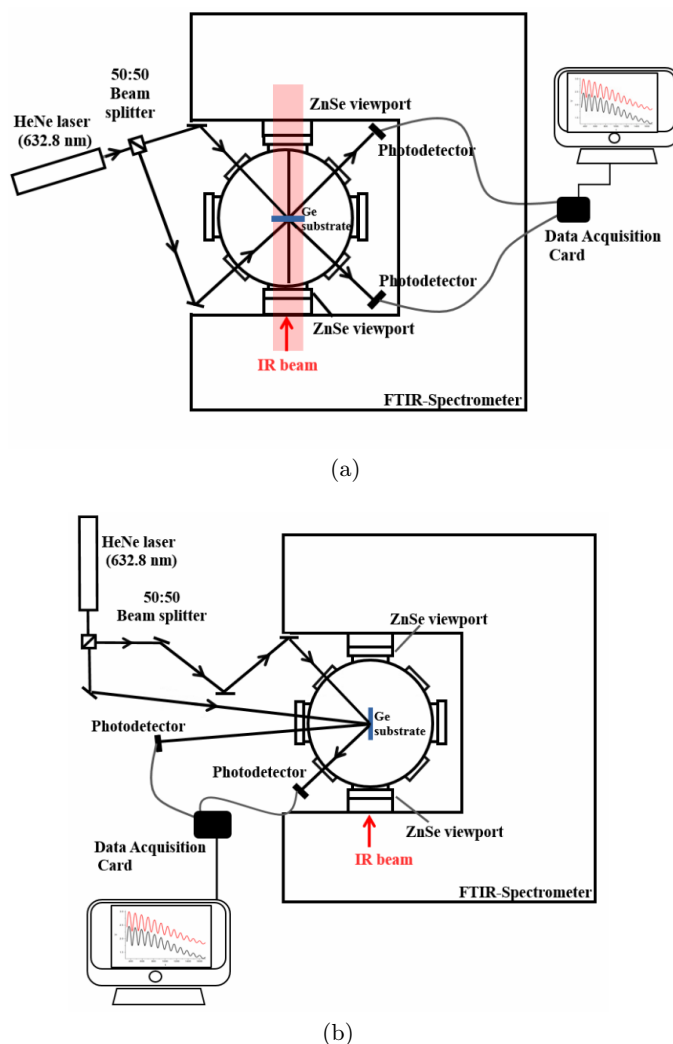


Fig. 1. Schematic picture of the new IRASIS setup. (a) Configuration in which the IR and thickness measurements are performed simultaneously. The laser beam impinges on the substrate at an angle $45 \pm 3^\circ$ on one side of the substrate and $42 \pm 3^\circ$ on the other side. (b) Configuration for refractive index measurements only: the substrate is rotated by 90° and the laser hits the substrate at two different angles (for this work $\theta_0 = 5.8^\circ \pm 0.5^\circ$ and $\theta_1 = 50.0^\circ \pm 0.5^\circ$).

both detectors. Figure 1a shows the experimental configuration for simultaneous acquisition of infrared spectra and laser interference measurements (in the measurements described here $\theta_0 = 45^\circ \pm 3^\circ$ and $\theta_1 = 42^\circ \pm 3^\circ$).

The refractive index of pure methylamine ice at 15 K is derived by a double-laser interference technique that employs two laser beams hitting the ice sample (in a same spot) at different angles and generating two interference patterns (for details, see Tempelmeyer & Mills Jr 1968; Romanescu et al. 2010; Beltrán et al. 2015; Hudson et al. 2017). The period of the interference patterns and the incidence angles of the two laser beams are related to the refractive index of the ice by:

$$n = \sqrt{\frac{\sin^2 \theta_0 - \gamma^2 \sin^2 \theta_1}{1 - \gamma^2}}, \quad (2)$$

where $\gamma = \frac{T_1}{T_0}$ is the ratio between the two periods T_1 and T_0 of the interference signals generated by the two laser beams

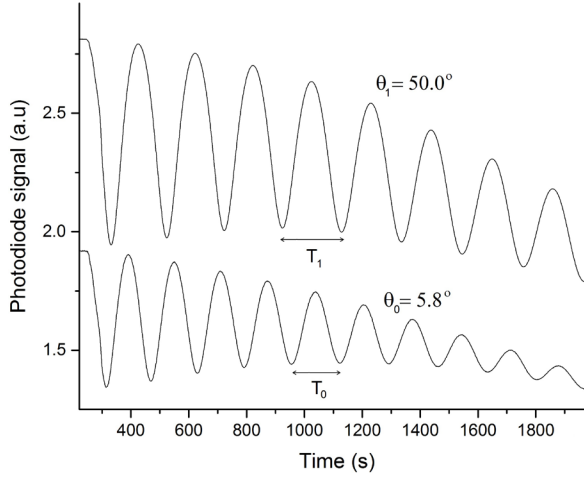


Fig. 2. Interference pattern obtained during ice growth. In this work, the employed laser beams hit the substrate at angles $\theta_0 = 5.8^\circ \pm 0.5^\circ$ and $\theta_1 = 50.0^\circ \pm 0.5^\circ$.

(see Fig. 2), impacting on the substrate at angles θ_1 and θ_0 , respectively.

Since the refractive index measurements are more sensitive to the accuracy in the incident angle around 50° , these measurements are performed using a different optical configuration, in which the sample holder is rotated by 90° (Fig. 1b). In this configuration, the uncertainty in the angle is smaller, as the angle can be determined by measuring the laser beam over larger distances from the substrate. In this work, the laser beams hit the substrate at angles $5.8^\circ \pm 0.5^\circ$ and $50.0^\circ \pm 0.5^\circ$.

2.1. Ice samples

Under interstellar ice conditions, CH_4 and NH_3 are embedded in a H_2O rich matrix, formed at very early stages of stellar evolution, still in the molecular cloud stage (Boogert et al. 2015; Linnartz et al. 2015; Fedoseev et al. 2015; Qasim et al. 2020). To simulate more realistic astronomical conditions, the studied ices are prepared by mixing methylamine with H_2O , CH_4 , and NH_3 , in binary, tertiary, and quaternary mixtures containing these molecules.

To analyze the effects of methylamine dilution on the IR spectral features, three different concentrations were prepared: 1:5, 1:10, and 1:20, which means that for each methylamine molecule in the ice sample, there are 5, 10, or 20 molecules of the other ice component(s). The deposition rates (and consequently the column densities) of the different species in the ices are derived by considering the weighted deposition rate of all the species in the gaseous mixture. Based on previous work (Terwisscha van Scheltinga et al. 2018), the uncertainty in this approach is estimated to amount to 10 percent for the accuracy with which a gas mixture can be prepared, and, upon deposition, another 10 percent uncertainty is added to account for changes in the deposition rate of the individual components. This results in propagated uncertainties of 14, 17 and 20 percent in the column densities of the two, three, and four-component ices. For the uncertainty in the ratio between two species in the deposited ice, this number translates into values of 20, 24, and 28 percent, respectively. The IR spectra of all the ice samples are recorded from 15 to 160 K. The desorption of matrix components during the ice heating changes the relative methylamine concentration in the sample, causing methylamine bands to appear stronger or

Table 1. Characteristics of the analyzed ice samples (composition, mixing ratios, methylamine column density, and temperature range).

Mixture	Mixing ratios	$N_{\text{CH}_3\text{NH}_2}$ (10^{17} cm^{-2})	Temperature range (K)
$\text{CH}_3\text{NH}_2:\text{H}_2\text{O}$	1:5	4.5 ± 0.6	15–150
$\text{CH}_3\text{NH}_2:\text{H}_2\text{O}$	1:10	2.5 ± 0.3	15–150
$\text{CH}_3\text{NH}_2:\text{H}_2\text{O}$	1:20	1.3 ± 0.2	15–150
$\text{CH}_3\text{NH}_2:\text{CH}_4$	1:5	3.7 ± 0.5	15–45
$\text{CH}_3\text{NH}_2:\text{CH}_4$	1:10	2.0 ± 0.3	15–45
$\text{CH}_3\text{NH}_2:\text{CH}_4$	1:20	1.0 ± 0.1	15–45
$\text{CH}_3\text{NH}_2:\text{NH}_3$	1:5	4.4 ± 0.6	15–115
$\text{CH}_3\text{NH}_2:\text{NH}_3$	1:10	2.4 ± 0.3	15–115
$\text{CH}_3\text{NH}_2:\text{NH}_3$	1:20	1.3 ± 0.2	15–115
$\text{CH}_3\text{NH}_2:\text{H}_2\text{O}:\text{CH}_4$	1:5:5	2.2 ± 0.4	15–150
$\text{CH}_3\text{NH}_2:\text{H}_2\text{O}:\text{CH}_4$	1:10:10	1.2 ± 0.2	15–150
$\text{CH}_3\text{NH}_2:\text{H}_2\text{O}:\text{NH}_3$	1:5:5	2.5 ± 0.4	15–150
$\text{CH}_3\text{NH}_2:\text{H}_2\text{O}:\text{NH}_3$	1:10:10	1.3 ± 0.2	15–150
$\text{CH}_3\text{NH}_2:\text{CH}_4:\text{NH}_3$	1:5:5	2.2 ± 0.4	15–115
$\text{CH}_3\text{NH}_2:\text{CH}_4:\text{NH}_3$	1:10:10	1.2 ± 0.2	15–115
$\text{CH}_3\text{NH}_2:\text{H}_2\text{O}:\text{CH}_4:\text{NH}_3$	3:10:10:10	2.3 ± 0.4	15–150

Notes. For more information on the uncertainty of the ice mixtures, see Sect. 2.1.

have a different profile because of new intermolecular interactions in the ice. Due to these changes and the fact that we do not have precise information about the new mixing ratio, quantitative analyses of the methylamine bands are made until the majority of the ice matrix components have desorbed. The composition, ice mixing ratio, column density of methylamine in the ice, and temperature range of all studied samples are listed in Table 1.

2.2. Band strength of the methylamine IR features

As described previously, the refractive index of the pure methylamine ice can be derived through a double laser interference technique. A representative data obtained in this way is shown in Fig. 2. The procedure to obtain the periods of the generated signals (T_0 and T_1 for Eq. (2)) and the position of the constructive interference for thickness measurements (Eq. (1)) are made using a personal Python script. The interference pattern is initially baseline corrected using a Savitzky-Golay filter, followed by the adjust of a sine function, whose periods are employed to calculate n (Eq. (2)). Other methods for deriving the period from an interference pattern consist of measuring the number of fringes in a large interval of time, averaging a large number of individual periods, or adjusting the signal using a multiparameter function containing polynomial terms and a periodic term modulated by an exponential decay. These methods yield refractive index values consistent with the method used in this work within their uncertainties. In this work, the refractive index for pure methylamine ices is measured at 15 K (amorphous) and at 123 K (crystalline), being these values 1.30 ± 0.01 and 1.40 ± 0.01 , respectively. The later value was measured for calculating the molar refraction of methylamine, necessary for deriving the ice density through the Lorentz-Lorenz relation, as described below.

A pure ice's column density (in molecules per cm^2) as function of its thickness can be written as:

$$N = \frac{d \rho N_A}{M}, \quad (3)$$

Table 2. Calculated IR band strengths (A) of amorphous methylamine ice at 15 K.

Peak position (cm ⁻¹)	Integrated region (cm ⁻¹)	Assignment	A (10 ⁻¹⁸ cm molec ⁻¹)
2881.3	2893–2870	CH ₃ antisymmetric stretch	2.6 ± 0.5
2791.8	2825–2765	CH ₃ symmetric stretch	3.8 ± 0.6
1478.6	1500–1467	CH ₃ antisymmetric def.	1.1 ± 0.2
1455.0	1467–1440	CH ₃ antisymmetric def.	0.7 ± 0.1
1420.3	1432–1407	CH ₃ symmetric def.	0.20 ± 0.03
1159.2	1215–1130	CH ₃ rock	1.5 ± 0.2

where d is the sample thickness (in cm), ρ is the mass density (in g cm⁻³), N_A is the Avogadro's number, and M is the ice component's molar mass (in g mol⁻¹). Using Eq. (3) and the Lambert-Beer law, the band strength (A) of a given IR feature is given by (Yamada & Person 1964):

$$A = \frac{2.3 M}{\rho d N_A} \int_{\nu} \text{abs}_{\nu} d\nu, \quad (4)$$

where A is given in cm molecule⁻¹, and $\int_{\nu} \text{abs}_{\nu} d\nu$ is the integrated absorbance of the band (i.e., the band area).

The pure methylamine band strength measurements are performed by growing relatively thin ices (typically 2–4 fringes in the interference pattern) and recording spectra at 1.0 cm⁻¹ resolution. The ice thickness and area of the IR bands are monitored simultaneously, and a linear adjustment of the thickness × time and band area × time yields good linear relations (R^2 bigger than 0.98). By using the slope of such linear relations and Eq. (4), the band strength of a given feature can be calculated as:

$$A = \frac{2.3 M \alpha}{\rho N_A \beta}, \quad (5)$$

where α is the variation of integrated band absorbance (band area) in time, and β is the variation of ice thickness in time. In the derivation of the pure ice band strengths, the methylamine mass density (ρ in Eq. (5)) is the main source of uncertainty. To the best of our knowledge, the density of amorphous methylamine ice has not been reported in the literature, only the value for orthorhombic CH₃NH₂ at 123 K is available (Atoji & Lipscomb 1953). The methylamine density at 15 K can be estimated using the Lorentz-Lorenz relation in a molar version:

$$R_M = \frac{M}{\rho} \left(\frac{n^2 - 1}{n^2 + 2} \right) \quad (6)$$

where R_M , M , ρ , and n are respectively the molar refraction, the molar mass, the mass density, and the refractive index of the molecule under analysis. The molar refraction can be estimated from the individual chemical bonds' molar refraction (Denbigh 1940; Hudson et al. 2020) or from Eq. (6) using the density and refractive index for crystalline methylamine at 123 K. Following the second approach, Eq. (6) yields $R_M = 8.86$ cm³ mol⁻¹ when $n = 1.40 \pm 0.01$ and $\rho = 0.85$ g cm⁻³ (from Atoji & Lipscomb 1953) are employed. Using this molar refraction value, a pure amorphous methylamine density of 0.66 cm⁻³ is obtained. This density is used in Eq. (5) for deriving methylamine band strengths, and in the case that a more accurate measurement of the amorphous methylamine density becomes available, the

bands strengths derived here can be re-scaled. Table 2 shows the calculated methylamine band strengths and the wavelength region that is used for the calculation of the band areas. All the spectra are baseline corrected before area calculations.

2.3. Relative band strengths

The light absorption profile of a molecule changes depending on the chemical environment surrounding the species. This is well known from studies analyzing the IR band profiles of molecules in different liquid or solid mixtures. Once the band profile changes, the IR apparent band strengths may change significantly. For a better quantification of methylamine in astrophysical ice analogs, the relative band strengths are calculated. In this work, the relative band strength (η) is the ratio between the apparent band strength of a given band when embedded in an ice mixture and the corresponding band strength in the pure ice:

$$\eta = \frac{A'}{A}, \quad (7)$$

where A' is the apparent band strength for a band in a given mixture and A is the band strength of the same band in pure methylamine ice at 15 K. The apparent band strength values and their uncertainties for the methylamine bands are graphically displayed in Appendix A.

3. Results and discussion

This section presents a set of representative mid-IR spectra of the methylamine-containing ices analyzed in this work. Changes in the IR absorbance profile of pure methylamine and mixed ices are described, and some ideas concerning the origins of these changes are pointed out. The complete data set is available from the Appendices. In Appendix A, spectra showing the selected methylamine bands in ice mixtures are presented for selected temperatures. The FWHM values versus peak positions are graphically shown for different ice mixtures and temperatures. The relative band strength values (see Eq. (7)) for different matrices are also given. The peak positions and FWHMs of the selected bands are organized in Tables B1–B15, and the integrated absorbance of the methylamine in different ice mixtures is listed in Tables C1–C15 (see notes in Appendices B and C).

This section is organized as follows: firstly, the overall spectra of methylamine ice in amorphous (15 K) and crystalline (101 K) form are presented. According to data found in the literature, the infrared features are assigned to the corresponding vibrational modes, and the most prominent features in the spectra

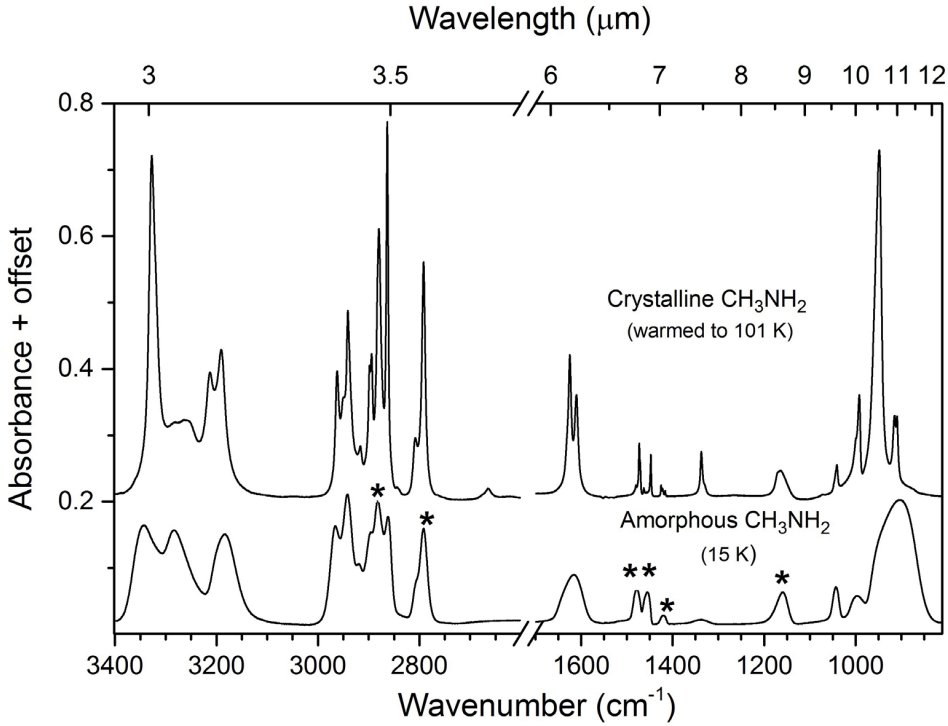


Fig. 3. Infrared spectra of amorphous (bottom spectrum) and crystalline (top spectrum) methylamine ice acquired with resolution of 0.5 cm^{-1} in the range from $3400\text{--}850\text{ cm}^{-1}$. The methylamine peaks chosen for in-depth characterization are marked with an asterisk.

are described. In the next subsections, profiles of specific methylamine bands are analyzed. These infrared features are selected based on a minimal overlap with bands of abundant molecules detected in water-rich interstellar ices (i.e., CO_2 , CH_4 , and NH_3).

The actual composition of interstellar ices is far more complex than the mixtures presented here. Also, infrared astronomical data exhibit absorption features from the dust material. Thereby, methylamine features may be hidden by absorption of species other than H_2O , NH_3 , and CH_4 , in particular molecules with similar functional groups. In order to maintain our analysis feasible, only a few other typically more abundant species, such as methanol, are explicitly taken into account.

3.1. Pure methylamine ice

Figure 3 shows the spectra of methylamine ice deposited at 15 K (amorphous) and heated to 101 K (crystalline). The pure CH_3NH_2 ice crystallizes around 100 K, and upon heating, this phase transition is spotted by the abrupt sharpening and splitting of the IR absorption bands. These changes are the result of a more organized ice structure, which reduces the diversity of molecular orientations. Table 3 lists the peak positions for amorphous (15 K) and crystalline (101 K) methylamine ice measured in this work, along with their tentative assignments (based on the work of Durig & Zheng 2001) and literature values for methylamine ices.

The $3000\text{--}2750\text{ cm}^{-1}$ region contains the methylamine ice features assigned to the CH_3 stretch mode and overtones of the CH_3 deformation modes. In pure methylamine, the bands in this region are strong, including the overtone modes, whose intensities are enhanced due to Fermi resonance (Durig et al. 1968; Wolff 1970; Lavalley & Sheppard 1972).

The peaks at 1455.0 and 1478.6 cm^{-1} are assigned to the CH_3 antisymmetric deformation mode. By warming up the ices, the peak positions do not change significantly until the ice

crystallizes. Upon the phase transition, both peaks narrow abruptly: the FWHM changes from 16.8 and 13.8 cm^{-1} at 15 K to 4.7 and 2.7 cm^{-1} at 100 K for the 1478.6 and 1455.0 cm^{-1} features, respectively (see Fig. 3 and Table B.7).

In pure methylamine ice, the symmetric deformation of the CH_3 group appears as a single feature at 1420.3 cm^{-1} (Fig. 3). As the temperature increases, the peak position and FWHM do not change significantly at temperatures lower than 100 K. At 100 K, the sample crystallizes, and an abrupt narrowing and shift to lower wavenumbers are observed. The narrowing of the CH_3 symmetric deformation band peaks reveals three features, at 1416.5 , 1422.0 , and 1425.4 cm^{-1} , with the former feature being the strongest one.

The feature assigned to the methylamine CH_3 rock vibrational mode appears at 1159.2 cm^{-1} in pure methylamine at 15 K and shifts to higher wavenumbers when the ice is heated, peaking at 1164 cm^{-1} at 100 K. The warming of the pure ice causes a slight narrowing of this peak, changing the FWHM from 28.4 at 15 to 26.2 cm^{-1} at 100 K. Unlike other methylamine bands, no strong and abrupt sharpening and increase in intensity are observed upon crystallization.

Methylamine presents a strong feature at 903.5 cm^{-1} assigned to the ν_9 mode. Upon crystallization, this feature sharpens and is one of the most strong features in the methylamine spectrum. Despite being a strong feature, this peak is not characterized throughout this work, since it overlaps with the broad libration mode of H_2O ice (around 760 cm^{-1}), being not easy to disentangle in a complex ice mixture. Since the goal of this work is characterizing features that present less overlapping with such abundant ice components, the band at 903.5 cm^{-1} was not chosen for a more in-depth investigation.

In the upcoming sections, we describe the morphology of methylamine features in pure and mixed ices in more detail. The features selected for in-depth investigation are the CH_3 rock mode around 1159 cm^{-1} , the CH_3 symmetric deformation around 1420 cm^{-1} , the CH_3 antisymmetric deformation modes that give

Table 3. Vibrational modes of pure methylamine ice.

Mode	Assignment	Amorphous ^(a)	Crystalline ^(a)	Solid ^(b)	Solid ^(c)
		15 K	101 K	10 K	120 K
ν_{10}	NH ₂ antisymmetric stretch	3342.8	3327.6	3348	3332
ν_1	NH ₂ symmetric stretch	3283.4		3287	3260
		3183.2	3212.8	3189	3191
			3190.6		
ν_{11}	CH ₃ antisymmetric stretch	2965.3	2962.4	2969	
		2941.9	2941.1	2945	2942
		2896	2898.2	2899	
ν_2	CH ₃ antisymmetric stretch		2894.1		
		2881.3	2879.9	2884	2881
		2862.1	2863.3	2865	
ν_3	CH ₃ symmetric stretch	2791.8	2791.9	2794	2793
ν_4	NH ₂ def.	1616.1	1625.0	1618	1651
			1472.8		
ν_{12}	CH ₃ antisymmetric def.	1478.6	1480.1	1479	1500
ν_5	CH ₃ antisymmetric def.		1610.5		
		1455.0	1447.8		
ν_6	CH ₃ symmetric def.		1463.0		
		1420.3	1425.4	1421	1441
			1422.0		
			1416.5		
ν_{13}	CH ₃ rock/NH ₂ twist	1339.1	1337.4	1339	1353
ν_7	CH ₃ rock	1159.2	1164.3	1161	1182
ν_8	CN stretch	1043.3	1040.9	1045	1048
ν_{14}	CH ₃ rock/NH ₂	996.8	991.7	997	1005
ν_9	NH ₂ wag	903.5	948.1	931	955
			914.8		
			909.5		

References. ^(a)This work, ^(b)Oba et al. (2014), ^(c)Durig et al. (1968).

rise to the bands around 1455.0 and 1478.6 cm⁻¹, the CH₃ symmetric stretch band, around 2791.8 cm⁻¹, and the CH₃ antisymmetric stretch band, around 2881.3 cm⁻¹. These six peaks are labeled with an asterisk in Fig. 3.

3.2. Mixed methylamine ices

3.2.1. CH₃ rock – 1159.2 cm⁻¹

In the binary CH₃NH₂:H₂O ice mixtures, the band due to the CH₃ rock vibrational modes shifts toward higher wavenumbers, peaking at 1176.8, 1177.5, and 1178.3 cm⁻¹ in the 1:5, 1:10, and 1:20 mixtures, respectively (see Tables B.1, B.2, B.3, and Figs. 4, A.1, and A.2). By warming the CH₃NH₂:H₂O mixtures, this methylamine band narrows by 1–3 cm⁻¹. In the binary mixtures with CH₄, the peak shifts to lower wavenumbers with an increasing CH₄ ratio. However, upon heating of the CH₃NH₂:CH₄ mixtures, the peak position shifts to higher wavenumbers, and the FWHM increases. These shifts can be due to rearrangements inside the ice and hydrogen bonds forming between methylamine molecules. In the CH₃NH₂:CH₄(1:20) ice, this feature is visible but it is too weak for quantitative analysis (Fig. A.2).

In the NH₃-containing samples, the methylamine CH₃ rock band overlaps with the strong feature of the ammonia umbrella vibration (around 1070 cm⁻¹), appearing as a weak shoulder in the ammonia feature (see Figs. 4, A.1–A.4 – in some of the panels, the position of the shoulder, when visible, is marked with a

dashed vertical line). This band can be observed as a shoulder in binary mixtures with a ratio 1:5, some of the 1:10 mixtures (including the CH₃NH₂:H₂O:CH₄:NH₃(3:10:10:10)) but is almost absent in the 1:20 mixtures. The shoulder becomes more prominent at higher temperatures due to the narrowing of the ammonia band.

3.2.2. CH₃ symmetric deformation – 1420.3 cm⁻¹

In all the mixed ices, the CH₃ symmetric deformation band appears at higher wavenumbers when compared to pure methylamine ice, shifted by around 5 cm⁻¹ (see Tables B.4–B.6 and the rightmost feature in the panels of Figs. 5, A.5–A.8). The more substantial shifts are observed for the H₂O containing mixtures, for which this feature appears between 1424 and 1425 cm⁻¹. In all the ice samples, this band does not overlap with any bands from H₂O, CH₄, and NH₃. Also, this feature is distinguishable in all the samples with exception of the CH₃NH₂:CH₄(1:20) ice, where it appears as a weak feature.

The peak intensity of the CH₃ symmetric deformation is enhanced in the water-containing mixtures. From Figs. 5, A.5, and A.6, it is possible to notice that the peak height of this feature in the H₂O-containing matrices is comparable to the intensity of the CH₃ antisymmetric deformation features, located at 1455.0 and 1478.6 cm⁻¹. In the mixtures without water and the pure methylamine ice, the peak height of the CH₃ symmetric deformation is less than half of the intensity of the CH₃ antisymmetric

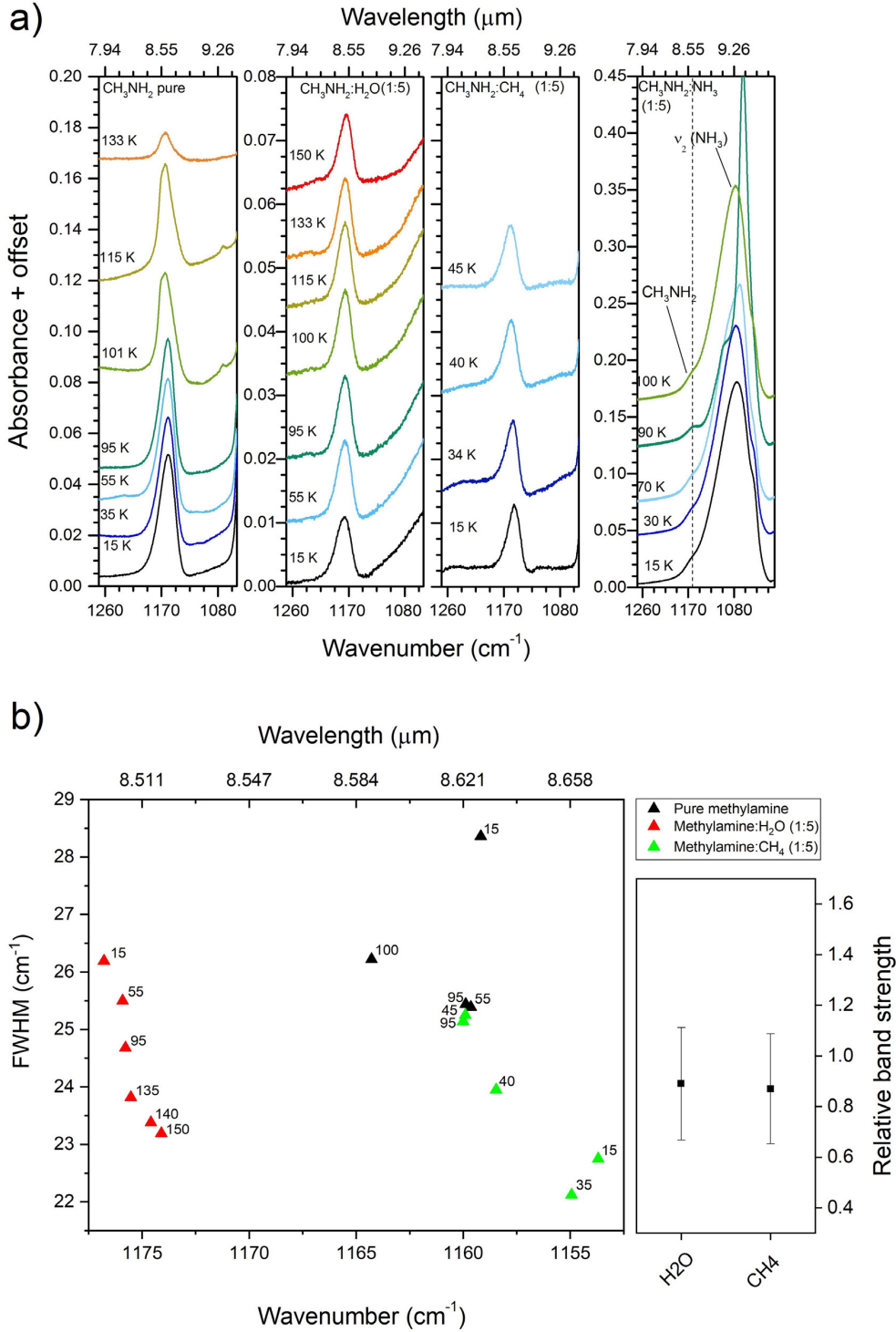


Fig. 4. (a) Infrared profile of the CH_3 rock vibrational mode of CH_3NH_2 , around 1159 cm^{-1} , in different ices, from left to right: pure CH_3NH_2 , $\text{CH}_3\text{NH}_2:\text{H}_2\text{O}(1:5)$, $\text{CH}_3\text{NH}_2:\text{CH}_4(1:5)$, and $\text{CH}_3\text{NH}_2:\text{NH}_3(1:5)$. The first and the last panels are displayed at a different Y-scale. In the last panel the CH_3NH_2 feature (whose position is indicated by the dashed line) appears as a shoulder in the ammonia ν_2 band (umbrella mode). (b) Left panel: peak position vs. FWHM for the CH_3 rock band in the ice mixtures displayed in a. Different mixtures are indicated by different colors, and the ice temperatures are marked in the graph. Right panel: relative band strength of the CH_3 rock vibrational mode in different ice mixtures at 15 K.

deformation features. The enhancing in strength is also noticed in the apparent band strength of this feature, that is around three times higher in $\text{CH}_3\text{NH}_2:\text{H}_2\text{O}$ ice mixtures when compared to the values for pure methylamine ice (see panels displaying the relative band strengths in Figs. 5c, A.5c, and A.6c).

3.2.3. CH_3 antisymmetric deformation – 1455.0 and 1478.6 cm^{-1}

In the ice mixtures, the feature at 1455 cm^{-1} peaks at higher wavenumbers when compared to the pure methylamine ice, being the most significant shift observed in the water-containing

mixtures, in which it peaks between $1462\text{--}1464\text{ cm}^{-1}$ (Tables B.7–B.9 and the two peaks at higher wavenumbers on the panels of Figs. 5, A.5–A.8). By warming the ice mixtures, this peak position does not shift appreciably, but some notable trends in the binary mixtures are observed. With increasing temperature, the peak around 1455 cm^{-1} narrows in a water environment but becomes broader in CH_4 and NH_3 matrices. In the water-containing three-component ices and in the four-component ice, a decrease of FWHM is observed, following the trend for the $\text{CH}_3\text{NH}_2:\text{H}_2\text{O}$ ices (see Tables B.7–B.9).

The peak at 1478.6 cm^{-1} , also assigned to the CH_3 antisymmetric deformation mode, behaves differently from the peak

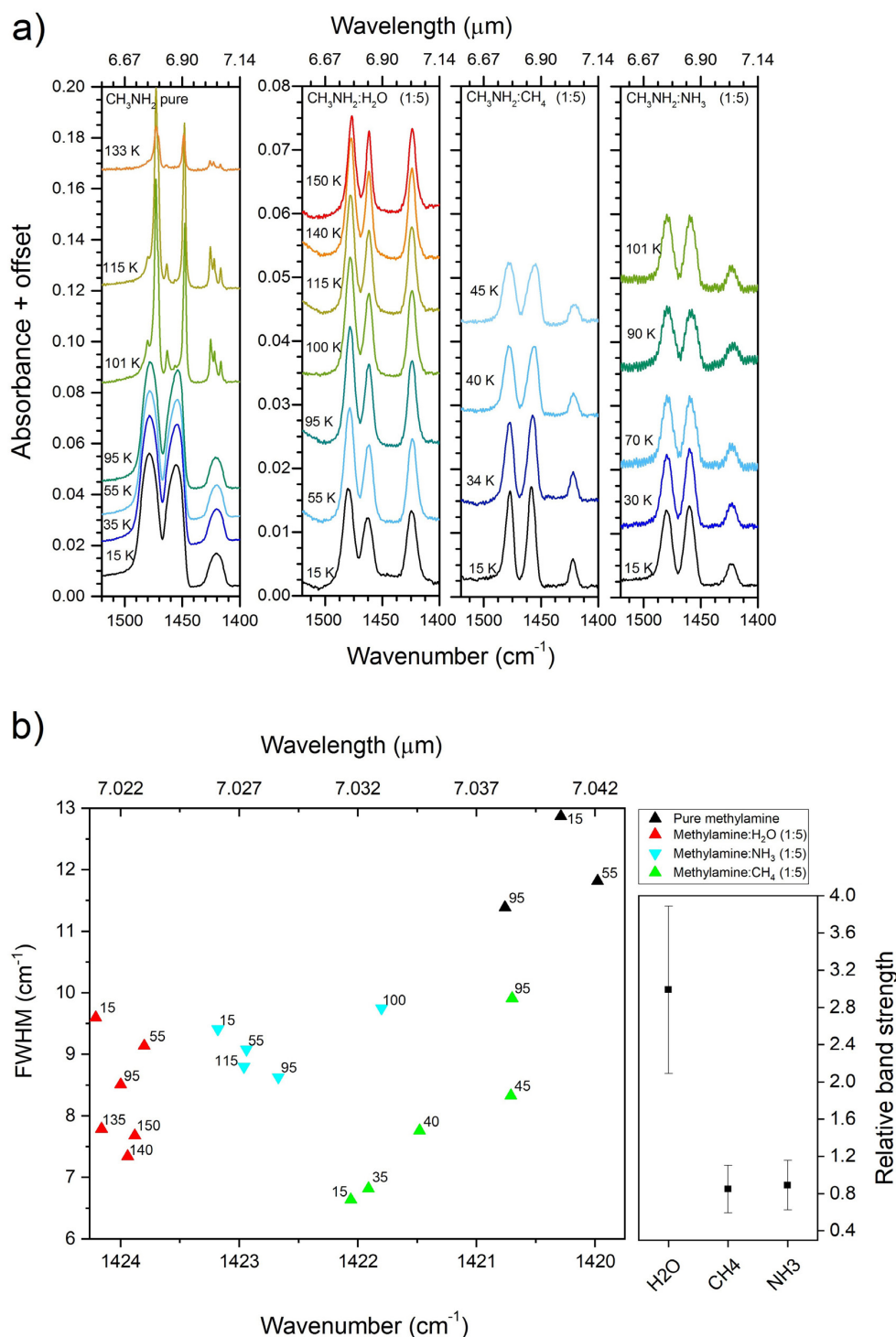


Fig. 5. (a) Infrared profile of the CH_3 antisymmetric deformation mode of CH_3NH_2 (the peaks around 1478.6 cm^{-1} and 1455.0 cm^{-1}) and the CH_3 symmetric deformation mode (around 1420 cm^{-1}), in different ices, from left to right: pure CH_3NH_2 , $\text{CH}_3\text{NH}_2:\text{H}_2\text{O}$ (1:5), $\text{CH}_3\text{NH}_2:\text{CH}_4$ (1:5), and $\text{CH}_3\text{NH}_2:\text{NH}_3$ (1:5). (b) Left panel: peak position vs. FWHM for the CH_3 symmetric deformation band (1420 cm^{-1}) in the ice mixtures displayed in a. Different mixtures are indicated by different colors, and the ice temperatures are marked in the graph. Right panel: relative band strength of the CH_3 symmetric deformation band (1420 cm^{-1}) in different ice mixtures at 15 K. Panels c and d: same as b for the CH_3 antisymmetric deformation modes, ν_5 and ν_{12} , at 1455 and 1478.6 cm^{-1} , respectively.

at 1455 cm^{-1} . In the two-component ices, this peak appears at higher wavenumbers in the H_2O and NH_3 matrices and lower wavenumbers in the CH_4 matrices (Tables B.7–B.9). In all the ice mixtures at 15 K, this feature shifts by a maximum of 2 cm^{-1} from the position in the pure methylamine ice. Upon heating, this peak slightly narrows and shifts toward low wavenumbers in H_2O and NH_3 and becomes broader and shifts toward higher wavenumbers in CH_4 . The broadening in the CH_4 matrix is probably due to the re-establishment of methylamine-methylamine interactions and is more pronounced when

CH_4 starts to desorb. In the 3 and 4 component mixtures, the changes in FWHM are not very pronounced, changing less than 2 cm^{-1} for all the mixtures with exception of the $\text{CH}_3\text{NH}_2:\text{CH}_4:\text{NH}_3$ ices.

Finally, the peak position, FWHM, and intensity of both features assigned to CH_3 antisymmetric deformation do not change dramatically after ice matrix crystallization compared to other methylamine bands. These peaks are also detectable even in the most diluted mixtures, offering perspective for use as a methylamine tracer.

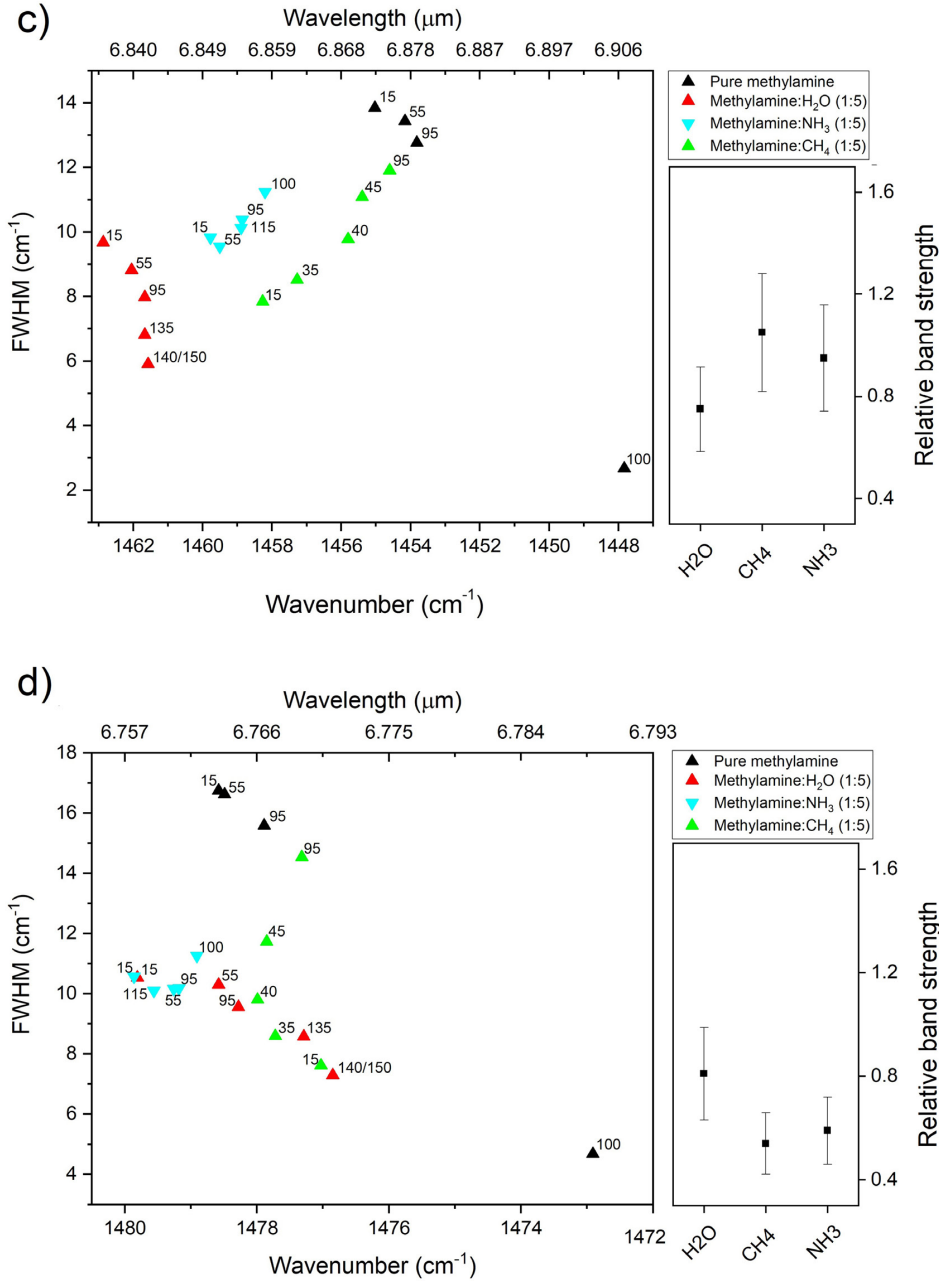


Fig. 5. continued.

3.2.4. The 3000–2700 cm^{-1} region

As previously shown, the IR spectrum of pure methylamine ice shows strong bands in the 3000–2700 cm^{-1} region (Fig. 3). As can be seen in the spectra of 1:5 mixtures of methylamine with H₂O, CH₄, and NH₃ (Fig. 6), bands in this region are blended, but some of the stronger features can be identified. The stretching modes and the overtones of deformation modes in this region have a similar profile as in most of the CH₃-bearing molecules, making it very difficult to look for particularities of the methylamine molecule. Figures 6, A.9–A.12 show the spectra in the 3000–2750 cm^{-1} region for all analyzed ice mixtures. The features that are chosen for characterization in this region are the CH₃ antisymmetric stretch (2881.3 cm^{-1}) and CH₃ symmetric stretch (2791.8 cm^{-1}) bands. The peak position and FWHM for these bands are measured and presented in Appendix B (Tables B10–B15).

In pure amorphous methylamine ice, the CH₃ symmetric stretch, around 2791.8 cm^{-1} , seems to have two overlapping components. In all the ice mixtures, the two components appear as two separate features (see Fig. 6). The component at higher wavenumbers occurs at the same position as the $\nu_2 + \nu_4$ combination mode of methane (around 2815 cm^{-1}), being difficult to separate (Fig. A.11 and A.12). The component at lower wavenumbers (around 2796 cm^{-1}) is visible in all ice spectra, although it appears as a weaker feature in the H₂O matrix.

In H₂O-containing ices, methylamine features in the 3000–2750 cm^{-1} region have an overall different profile compared to similar features in noncontaining H₂O matrices. This seems to be particular for the CH₃ vibrational modes, since such changes are not observed for the other vibrational modes. In CH₃NH₂:H₂O ices, the strongest peak in this region is due to a CH₃ antisymmetric stretch band located at 2898 cm^{-1} . This feature is visible in all the mixtures, and in matrices containing

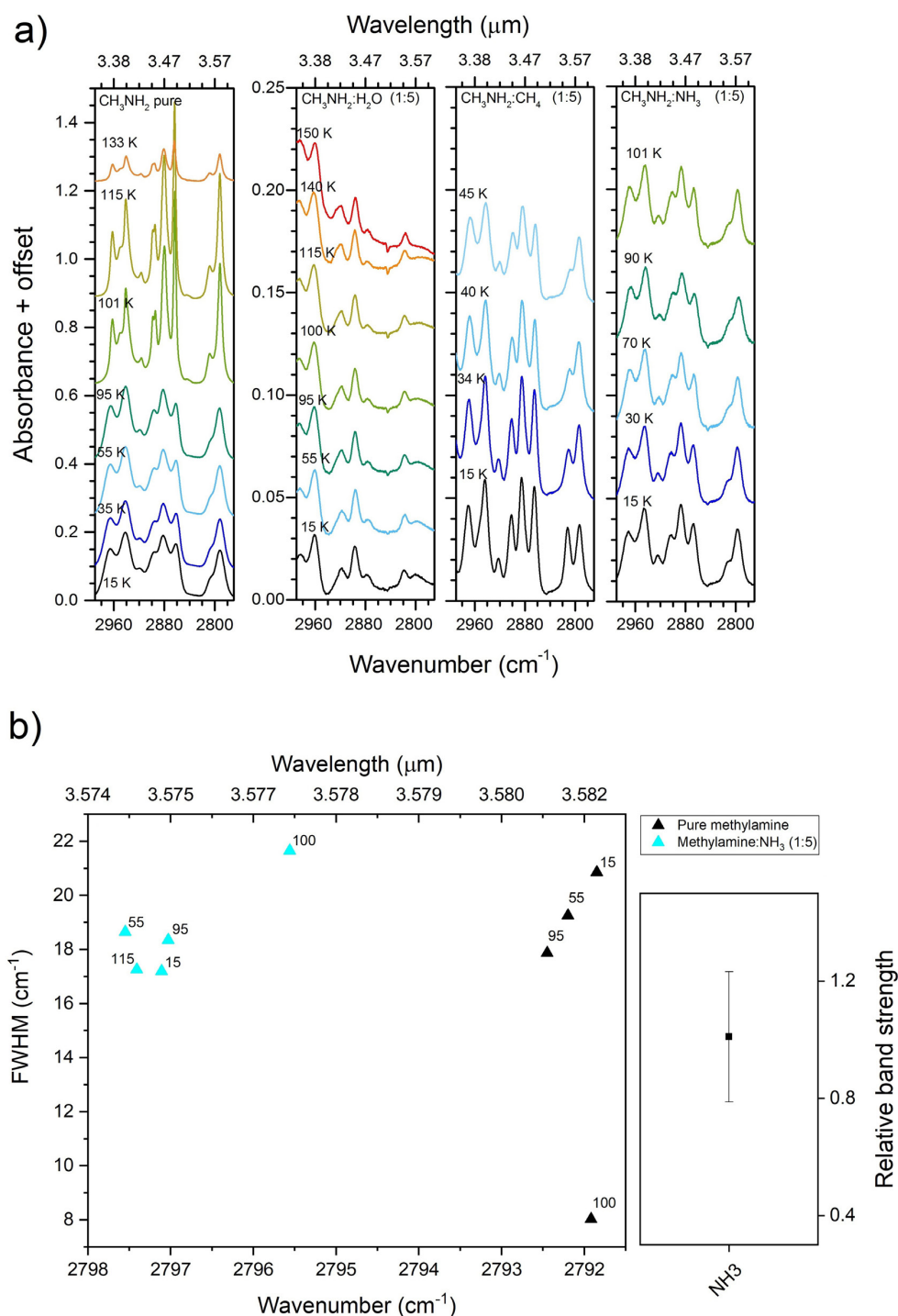


Fig. 6. (a) 2750–3000 cm^{-1} region with spectra of different ices, from left to right: pure CH_3NH_2 , $\text{CH}_3\text{NH}_2:\text{H}_2\text{O}$ (1:5), $\text{CH}_3\text{NH}_2:\text{CH}_4$ (1:5), and $\text{CH}_3\text{NH}_2:\text{NH}_3$ (1:5). The CH_3 anti-symmetric stretch mode of CH_3NH_2 (around 2881 cm^{-1}) and the CH_3 symmetric stretch mode of CH_3NH_2 (around 2792 cm^{-1}) are displayed in the panels. (b) *Left panel*: peak position vs. FWHM for the CH_3 symmetric stretch band in pure CH_3NH_2 and $\text{CH}_3\text{NH}_2:\text{NH}_3$ (1:5) ices. Different mixtures are indicated by different colors, and the ice temperatures are marked in the graph. *Right panel*: relative band strength of the CH_3 symmetric stretch band in pure CH_3NH_2 and $\text{CH}_3\text{NH}_2:\text{NH}_3$ (1:5) ices at 15 K. *Panel c*: same as b for the CH_3 antisymmetric stretch band (around 2881 cm^{-1}) in the ice mixtures displayed in a.

H_2O and CH_4 it partially overlaps with the ν_1 mode of CH_4 (Herrero et al. 2010). This overlap can be noticed in Figs. A.11 and A.12, where the 2898 cm^{-1} feature of CH_3NH_2 is wider than in H_2O , CH_4 and NH_3 matrices at temperatures below 50 K (Figs. 6, A.9 and A.10). Above 50 K, CH_4 starts to desorb and the remaining feature is similar to the 2898 cm^{-1} band observed in the $\text{CH}_3\text{NH}_2:\text{H}_2\text{O}$ ices. In $\text{H}_2\text{O}:\text{NH}_3:\text{CH}_3\text{NH}_2$ and $\text{H}_2\text{O}:\text{NH}_3:\text{CH}_3\text{NH}_2:\text{CH}_4$ ices, the bands in the 3000–2700 cm^{-1} region are difficult to resolve due to the overlap with broad absorption bands from $\text{H}_2\text{O}:\text{NH}_3$ hydrates (Moore et al. 2007). Some of the methylamine feature are clear in the mixtures with dilution 1:10, but appear as very weak peaks in dilution of 1:20 (Figs. A.10, and A.12).

A particularity of the ices in which methylamine is mixed in water is the appearance of a broad and strong feature centered around 2760 cm^{-1} . Figure 7 shows the feature in all the $\text{CH}_3\text{NH}_2:\text{H}_2\text{O}$ ice mixtures at 15 K. The appearance of such a broad profile is also noticed in the $\text{CH}_3\text{NH}_2:\text{CH}_4$ containing ices and in the $\text{CH}_3\text{NH}_2:\text{H}_2\text{O}:\text{NH}_3$ matrices, though this last is less perceptible due to the overlap with the broad ammonia hydrate feature centered around 2900 cm^{-1} . The 2760 cm^{-1} feature is clearly visible during the warming up of the ice mixtures and disappears only when methylamine desorbs from the ice. This band is likely due to the interaction of the N-H stretch mode of methylamine with the water O-H stretch mode and is possibly analogous to the ammonia hydrate feature observed in $\text{H}_2\text{O}:\text{NH}_3$.

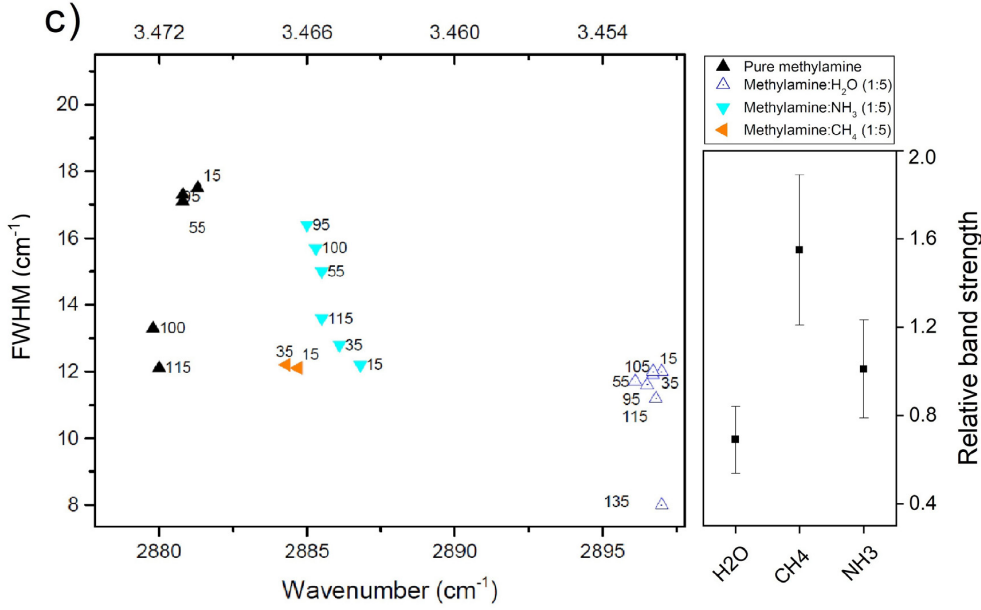


Fig. 6. continued.

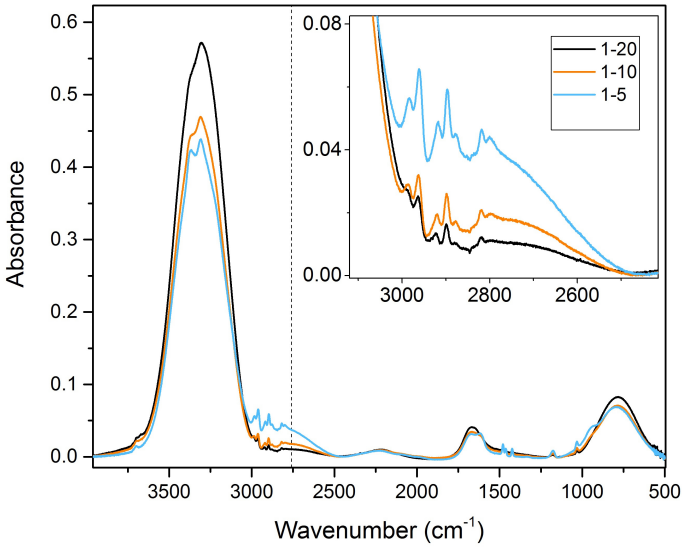


Fig. 7. Infrared spectra of CH₃NH₂:H₂O at ratios 1:5 (blue), 1:10 (orange) and 1:20 (black) at 15 K. The center of the broad feature at 2760 cm^{−1} is marked with a dashed line. *Top panel:* the zoom-in shows the 3100–2400 cm^{−1} region of the spectra.

ices (Dartois & d’Hendecourt 2001). Since this feature appears in a region of the mid-infrared spectrum that is free from strong absorption from abundant interstellar ice components, this band could indicate the presence of methylamine in H₂O-rich ices. However, other molecules containing an N-H group may show a similar absorption feature when embedded in H₂O matrix, which makes this band a not unambiguous tracer of any particular species.

4. Astronomical implications

In dense molecular clouds, CH₃NH₂ is likely to be formed in regions that are rich in atomic C, H, and N, that is, in the less dense regions, or early in the cloud’s life cycle, when also H₂O, CH₄, and NH₃ are formed (Ioppolo et al. 2021). Using a gas-grain astrochemical kinetic model (Garrod 2013) that involves

only non-energetic reactions, Ioppolo et al. (2021) showed that methylamine can be formed by barrierless reactions on the surface of interstellar icy grains during the prestellar core collapse. After the core collapse, the methylamine abundance in the ice mantle reaches 0.65 percent relative to H₂O, which is comparable to the abundance for solid CH₄ in the model. However, significantly higher solid CH₄ abundances (1–11 percent relative to H₂O; Öberg et al. 2008) are observed toward Young Stellar Objects (YSOs). This suggests that solid methylamine may also be detectable in dense clouds and YSO envelopes, and the data presented here offer a tool to do so.

The challenge for methylamine identification in interstellar ices is related to the fact that most of its strongest modes, explored in the previous sections, overlap with features from other abundant interstellar ice and dust components (e.g., CH₃OH, NH₃, silicates). In a realistic astronomical scenario, even the features that are easily identified in the laboratory will likely appear blended with bands from other species. The following sections describe the potential of solid methylamine absorption features as tracers of its presence in mid-infrared observations.

4.1. CH₃NH₂ in the 3–4 μm wavelength range

The methylamine features in the 3400–2500 cm^{−1} (2.94–4.0 μm) region have the advantage of being observable with ground-based telescopes at resolving power $R > 1000$, which is much higher than that for spectra in the 5–10 μm range observed with *Spitzer*/IRS ($R \sim 100$). Figure 8 shows a comparison of the CH₃NH₂:H₂O(1:10) ice spectrum at 15 K with low and high-mass YSO spectra obtained with Keck/NIRSPEC, VLT/ISAAC, and IRTF/SpEx (Boogert et al. 2008, Emerson & Boogert, in prep.). The peak positions of the methylamine features at 2898 cm^{−1} (3.451 μm), 2796 cm^{−1} (3.576 μm), and the broad feature at 2760 cm^{−1} (3.623 μm) are marked with vertical dashed lines. In H₂O mixtures, the band from the CH₃ antisymmetric stretch mode at 2898 cm^{−1} is the strongest methylamine feature in this region. It appears close to the CH₃ stretch bands from other organic molecules (e.g., acetaldehyde, ethanol) and the ν_1 mode of CH₄ observed in CH₄:H₂O ices, as discussed on the previous section. Still, at the high resolving power, this

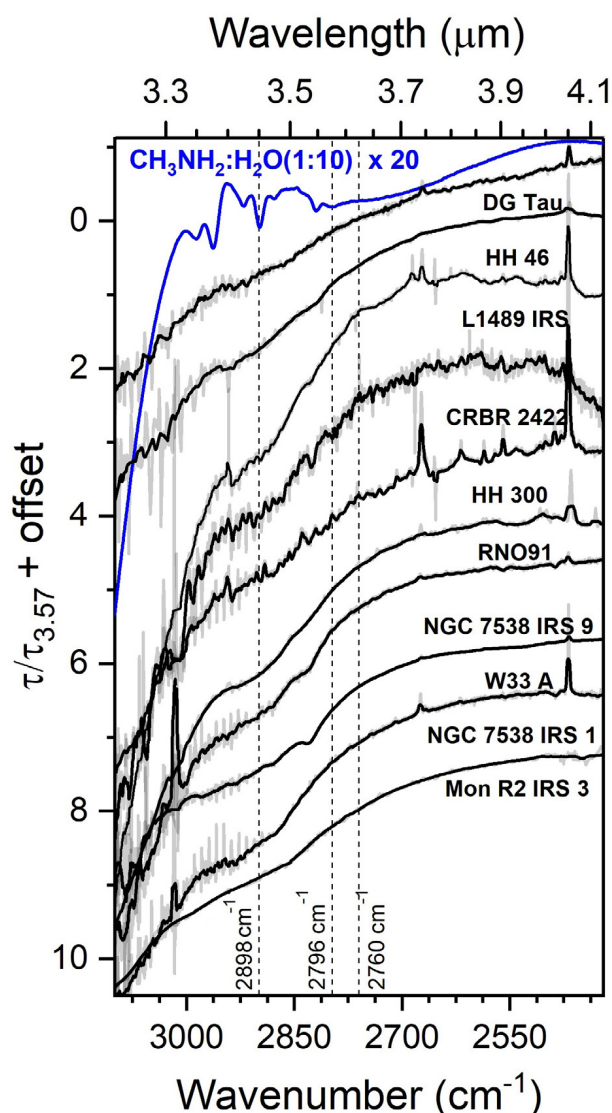


Fig. 8. Comparison between the IR profile of YSOs and the absorption spectra of the $\text{CH}_3\text{NH}_2:\text{H}_2\text{O}(1:10)$ ice at 15 K (top blue curve). All the YSO spectra are normalized in relation to the optical depth at 2800 cm^{-1} ($3.57\text{ }\mu\text{m}$). The gray lines are the original spectra and the black lines are the smoothed spectra. The smoothing uses a 15-point boxcar, that corresponds to a window of $4\text{--}6\text{ cm}^{-1}$ in the analyzed spectra. The position of the methylamine bands at 2898 , 2796 , and the feature at 2760 cm^{-1} are marked with dashed lines.

relatively narrow absorption feature is best suited to constrain the methylamine abundance. On the other hand, while the methylamine CH_3 antisymmetric stretch feature at 2796 cm^{-1} peaks at wavenumbers lower than most of the CH_3 stretch vibrations of abundant ice species, its strength is significantly suppressed in H_2O matrices.

The broad feature at 2760 cm^{-1} is observed in $\text{CH}_3\text{NH}_2:\text{H}_2\text{O}$ ice samples with a methylamine abundance as low as 5% relative to H_2O and is in a spectral region where few abundant interstellar ice molecules have absorption peaks. As can be seen from Fig. 8, such a broad feature centered at 2760 cm^{-1} is not promptly identified in the YSO spectra. We find that abundances estimates from this shallow band are strong limited by the baseline choice, and stronger constraints are obtained from the CH_3 antisymmetric stretch mode at 2898 cm^{-1} . In an alternative scenario where methylamine is embedded in an apolar ice environment,

the 2760 cm^{-1} feature would be absent. This seems an unlikely scenario since the formation routes of methylamine may well pass through NH_2 and CH_3 radicals in a H_2O matrix (Garrod 2013; Ioppolo et al. 2021).

4.2. CH_3NH_2 in the $5\text{--}8\text{ }\mu\text{m}$ wavelength range

In the $1700\text{--}1250\text{ cm}^{-1}$ ($\sim 5.9\text{--}8.0\text{ }\mu\text{m}$) range, airborne and space-based observations revealed a series of ice absorption features (Soifer et al. 1979; Schutte et al. 1996). Among the likely carriers of these features are many hydrocarbons and oxygen-bearing species, such as methanol (CH_3OH), formaldehyde (H_2CO), formic acid (HCOOH), acetaldehyde (CH_3CHO), ethanol ($\text{CH}_3\text{CH}_2\text{OH}$), the formate ion (HCOO^-) and others (Tielens et al. 1984; Schutte et al. 1996; Keane et al. 2001; Knez et al. 2005; Boogert et al. 2008, 2015; Bottinelli et al. 2010; Öberg et al. 2011). Some N-bearing molecules have also been proposed as possible carriers, for example, NH_3 , NH_4^+ (Schutte & Khanna 2003), HCN, and a few suggestions for larger molecules, such as acetonitrile (CH_3CN), urea (H_2NCONH_2) and formamide (HCONH_2 ; Raunier et al. 2004).

Figure 9 shows a comparison of the infrared spectra of methylamine-containing ices with the mid-IR spectra of YSOs obtained by *Spitzer*/IRS (Boogert et al. 2008). As can be seen from the figure, the NH_2 deformation mode and the CH_3 symmetric deformation mode of methylamine, around 1613 cm^{-1} and 1424 cm^{-1} , respectively, coincide with the strong features observed in the YSOs. Methylamine could thus be one of the species that contribute to both of these features. However, because the observed features result from a blending of many absorbing species, it is not possible to significant constrain the methylamine abundance. Future JWST observations at a resolving power of $R \sim 1000\text{--}3000$, more than an order of magnitude better than *Spitzer*, will be better suited to search for weak substructures, possibly providing better ice abundance constraints.

4.3. CH_3NH_2 in the $8\text{--}13\text{ }\mu\text{m}$ wavelength range

In the $1200\text{--}800\text{ cm}^{-1}$ ($\sim 8\text{--}12.5\text{ }\mu\text{m}$) region, the methylamine bands also overlap with features from abundant interstellar ice molecules. The CH_3 rock band, around 1159 cm^{-1} in pure methylamine, overlaps with the umbrella mode of NH_3 at 1070 cm^{-1} , appearing as weak shoulders in the laboratory spectra. Since ammonia is an abundant interstellar ice species, the band around 1159 cm^{-1} may not be suitable for methylamine identification. However, the presence of a shoulder at higher wavenumbers in the ammonia umbrella feature may be an indication of methylamine, but this again requires a high resolving power.

Methylamine also presents a strong peak around 903.5 cm^{-1} ($\sim 11.07\text{ }\mu\text{m}$), assigned to the ν_9 mode, that was not characterized in this work due to the overlap with the libration band of H_2O ice. This peak appears in the same region as the broad torsion mode band of CH_3OH (around 700 cm^{-1}) and a feature around 902.5 cm^{-1} ($11.08\text{ }\mu\text{m}$) observed in some YSOs that has been assigned to crystalline silicates Do-Duy et al. (2020). Investigations concerning COMs that can contribute to the astronomical feature around $11.08\text{ }\mu\text{m}$ should consider methylamine as a carrier candidate.

4.4. CH_3NH_2 abundances

With the currently available observations of YSO envelopes, the best estimate of the methylamine abundance is obtained from

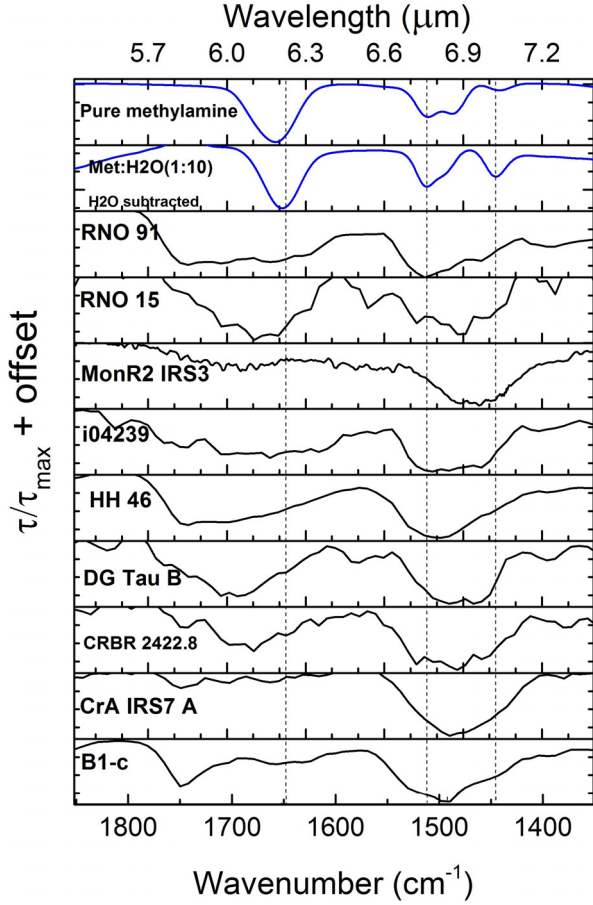


Fig. 9. Comparison between laboratory spectra of methylamine-containing ices and some *Spitzer*/IRS spectra of YSOs (with H₂O subtracted) in the 5.4–7.4 μm range (Boogert et al. 2008). *Two top panels:* spectra of pure methylamine ice at 15 K and the H₂O subtracted CH₃NH₂:H₂O(1:10) ice spectra at 15 K. The vertical dashed lines mark the peak positions of the bands in this mixture. The laboratory spectra are convolved with a Gaussian profile with FWHM corresponding to the *Spitzer*/IRS resolution ($R=100$). Both the laboratory and YSO spectra are normalized with respect to the 1612.9 cm⁻¹ (6.2 μm) feature for better visualization.

the 3000–2700 cm⁻¹ region (Fig. 8). No distinct feature due to methylamine is detected in the ground-based spectra, and the tightest upper-limit can be obtained from the feature around CH₃ antisymmetric stretch mode (around 2898 cm⁻¹ in CH₃NH₂:H₂O ices). The column density upper limit (N , in cm⁻²) of methylamine can be estimated from the FWHM and the band strength (A') of the 2898 cm⁻¹ feature:

$$N \leq \frac{\tau_v \times FWHM}{A'} \quad (8)$$

where $A' = 1.48 \times 10^{-18}$ cm molecule⁻¹ is the band strength for the 2898 cm⁻¹ feature and $FWHM = 11.8$ cm⁻¹ (adopting the value for the CH₃NH₂:H₂O(1:10) ice mixture, see Appendix A), and τ_v is the optical depth of the peak in the YSO spectra. For obtaining the optical depth, a local baseline is subtracted from the region around the 2898 cm⁻¹, and τ_v is taken as the maximum optical depth that is consistent with the absence of a peak centered at 2898 cm⁻¹ (with $FWHM = 11.8$ cm⁻¹) in the YSO spectra. Figure 10 shows an example of this procedure. The derived methylamine upper limits are shown in Table 4 along

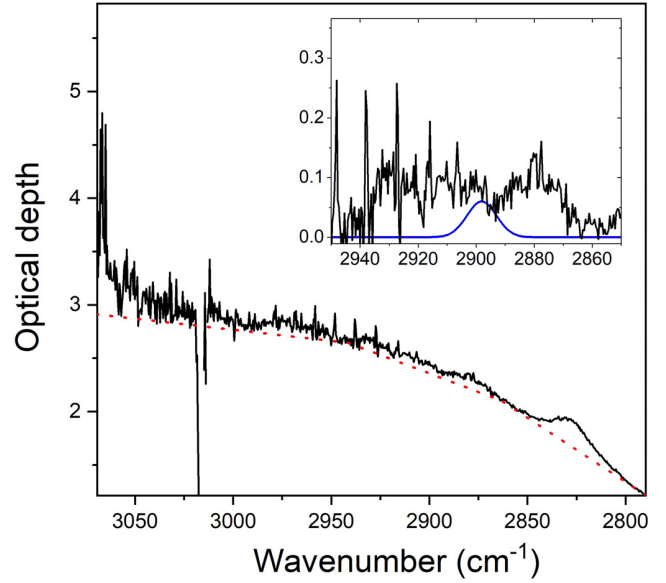


Fig. 10. Example of the adjustment of a local baseline in the W33A spectrum (red dotted line). The *top right panel* shows the subtracted spectra in the 2850–2950 cm⁻¹ region and the adjusted Gaussian feature (blue) expected from CH₃NH₂ in an H₂O matrix.

Table 4. Methylamine upper limits using the CH₃ antisymmetric stretch band at 2898 cm⁻¹.

Source	N(CH ₃ NH ₂) 10 ¹⁷ cm ⁻²	(% H ₂ O)
CRBR2422.8-342	≤6.7	16
L1489 IRS	≤2.3	5.3
HH46	≤8.4	10
DG Tau	≤1.7	7.4
RNO91	≤2.5	5.9
HH300	≤2.1	8.0
Mon R2 IRS 3	≤0.8	5.3
NGC 7538 IRS 1	≤0.8	3.1
NGC 7538 IRS 9	≤1.7	2.6
W33 A	≤4.2	3.4
Comet 67P ^{(a),(b)}	–	0.16
Model ^(c)	–	0.65

Notes. The methylamine abundances detected in the comet 67P/Churyumov-Gerasimenko and the predicted abundance for gas-grain astrochemical models of prestellar cores are also presented for comparison.

References. ^(a)Le Roy et al. (2015); ^(b)Altwegg et al. (2016); ^(c)Ioppolo et al. (2021).

with predicted values and the abundance observed in the Comet 67P.

As can be seen in Table 4, the methylamine upper limits values range from 2.6 to 16 percent in relation to water. The higher upper limits obtained for CRBR2422.8-342 and HH46 are a consequence of the lower S/N in the spectral region in comparison with some other objects (e.g., NGC 7538 IRS 1, NGC 7538 IRS 9, W33 A). For the YSO spectra with higher S/N, the abundance of methylamine is constrained to less than a few percent relative to H₂O, which is at the level of tentatively detected COMs (Öberg et al. 2011; Terwisscha van Scheltinga

et al. 2018). Still, the calculated values are higher than the methylamine abundance of 0.65 relative to H₂O from the gas-grain model presented by Ioppolo et al. (2021). This indicates that current IR observations of ices around YSOs are not sensitive enough to probe the solid methylamine budget, and so unable to significantly constrain the accuracy of methylamine formation models. Observations at higher spectral resolution and sensitivity across the full 3–10 μ m wavelength range with the JWST mission toward a wider variety of dense clouds and YSO targets should provide tighter constraints on the presence of COMs in the ices. The JWST early release program ICE AGE (McClure et al. 2018) targets a search for COM ice features in the wavelength domain studied here. The data presented in this work will support the interpretation of future data, helping to understand the chemical inventory of ices in star-forming regions.

5. Conclusions

This work reports a set of systematically measured infrared spectra of methylamine-containing ices in astronomically relevant conditions. The following methylamine features are selected for peak position and FWHM characterization in the studied ices: the CH₃ antisymmetric stretch band around 2881.3 cm⁻¹ (3.453 μ m), the CH₃ symmetric stretch band around 2791.8 cm⁻¹ (3.582 μ m), the CH₃ antisymmetric deformation bands around 1455.0 cm⁻¹ and 1478.6 cm⁻¹ (6.873 μ m and 6.761 μ m), the CH₃ symmetric deformation band around 1420.3 cm⁻¹ (7.042 μ m), and the CH₃ rock around 1159.2 cm⁻¹ (8.621 μ m). The mid-IR band strengths of pure methylamine ice (in the transmission mode) for the selected vibrational modes and the refractive index at 632.8 nm are, to the best of our knowledge, reported here for the first time. The relative band strengths of methylamine in the ice mixtures are also derived. These values are essential for estimating methylamine abundances in astronomical IR spectra. The main conclusions of this work are summarized below:

1. The interaction of methylamine with the H₂O matrix induces substantial changes in the methylamine absorption profile, such as: an enhancement in the strength of the CH₃ antisymmetric stretch (at 2898 cm⁻¹) in relation to other methylamine features in the 3000–2700 cm⁻¹ region, an enhancing in the CH₃ symmetric deformation mode (1425 cm⁻¹) strength, and the appearance of a broad and strong feature centered at 2760 cm⁻¹. This last feature appears in a region where few abundant interstellar ice species absorb, and therefore may also offer a tool to search for the presence of methylamine in interstellar ices.
2. The comparison of the methylamine-containing ices with mid-infrared spectra of some YSOs shows that despite some overlap between laboratory and astronomical data, no feature can be unambiguously assigned to methylamine. The methylamine bands are hard to be used as tracers due to blending with bands from other molecules. Even the bands that are clearly distinguishable in the laboratory ice data and are characterized in this work have a limited use to identify methylamine.
3. From the work presented here, upper limits for methylamine are derived based on the CH₃ antisymmetric stretch mode (at 2898 cm⁻¹ in CH₃NH₂:H₂O ices). In some of these YSOs, the methylamine abundance in respect to water is less than 4%.

With the upcoming JWST observations of ices, weaker solid-state features, not present in the available ice data, may be

revealed. Within the ICE AGE program several targets are envisaged to search for COM ice features in the wavelength domain studied here. The data presented in this work will support the interpretation of future JWST spectra, helping to understand the chemical inventory of ices in star-forming regions.

Acknowledgements. This work has been made possible through financial support by NOVA, the Netherlands Research School for Astronomy. We thank Dr. Jiao He for the helpful discussions about refractive index measurements and Dr. Will Rocha, Nicolas Suas-David, and Dr. Melissa McClure for helpful discussions. G.F. also acknowledges financial support from the Russian Ministry of Science and Higher Education via the State Assignment Contract FEUZ-2020-0038.

References

- Altwegg, K., Balsiger, H., Bar-Nun, A., et al. 2016, *Scie. Adv.*, **2**, e1600285
 Atoji, M., & Lipscomb, W. 1953, *Acta Crystallograph.*, **6**, 770
 Belloche, A., Menten, K., Comito, C., et al. 2008, *A&A*, **492**, 769
 Beltrán, M. D., Molina, R. L., Aznar, M. Á. S., Moltó, C. S., & Verdú, C. M. 2015, *Sensors*, **15**, 25123
 Bøgelund, E. G., McGuire, B. A., Hogerheijde, M. R., van Dishoeck, E. F., & Ligterink, N. F. W. 2019, *A&A*, **624**, A82
 Boogert, A. C. A., Pontoppidan, K. M., Knez, C., et al. 2008, *ApJ*, **678**, 985
 Boogert, A. C. A., Gerakines, P. A., & Whittet, D. C. B. 2015, *ARA&A*, **53**, 541
 Bossa, J.-B., Duvernay, F., Theulé, P., et al. 2009, *A&A*, **506**, 601
 Bossa, J.-B., Borget, F., Duvernay, F., Theulé, P., & Chiavassa, T. 2010, *J. Phys. Organic Chem.*, **23**, 333
 Bottinelli, S., Boogert, A. C. A., Bouwman, J., et al. 2010, *ApJ*, **718**, 1100
 Dartois, E., & d'Hendecourt, L. 2001, *A&A*, **365**, 144
 Denbigh, K. 1940, *Transac. Faraday Soc.*, **36**, 936
 Do-Duy, T., Wright, C. M., Fujiyoshi, T., et al. 2020, *MNRAS*, **493**, 4463
 Durig, J. R. & Zheng, C. 2001, *Struc. Chem.*, **12**, 137
 Durig, J., Bush, S., & Baglin, F. 1968, *J. Chem. Phys.*, **49**, 2106
 Elsila, J. E., Dworkin, J. P., Bernstein, M. P., Martin, M. P., & Sandford, S. A. 2007, *ApJ*, **660**, 911
 Fedoseev, G., Ioppolo, S., Zhao, D., Lamberts, T., & Linnartz, H. 2015, *MNRAS*, **446**, 439
 Förstel, M., Bergantini, A., Maksyutenko, P., Góbi, S., & Kaiser, R. I. 2017, *ApJ*, **845**, 83
 Fourikis, N., Takagi, K., & Morimoto, M. 1974, *ApJ*, **191**, L139
 Gardner, E. P., & McNesby, J. R. 1980, *J. Photochem.*, **13**, 353
 Garrod, R. T. 2013, *ApJ*, **765**, 60
 Garrod, R. T., Weaver, S. L. W., & Herbst, E. 2008, *ApJ*, **682**, 283
 Glavin, D. P., Dworkin, J. P., & Sandford, S. A. 2008, *Meteorit. Planet. Sci.*, **43**, 399
 Goesmann, F., Rosenbauer, H., Bredehöft, J. H., et al. 2015, *Science*, **349**, aaa9816
 Herbst, E. 1985, *ApJ*, **292**, 484
 Herrero, V. J., Gálvez, Ó., Maté, B., & Escribano, R. 2010, *Phys. Chem. Chem. Phys.*, **12**, 3164
 Hudson, R., Loeffler, M., & Gerakines, P. 2017, *J. Chem. Phys.*, **146**, 024304
 Hudson, R. L., Loeffler, M. J., Ferrante, R. F., Gerakines, P. A., & Coleman, F. M. 2020, *ApJ*, **891**, 22
 Ioppolo, S., Fedoseev, G., Chuang, K.-J., et al. 2021, *Nat. Astron.*, **5**, 197
 Kaifu, N., Morimoto, M., Nagane, K., et al. 1974, *ApJ*, **191**, L135
 Kayi, H., Kaiser, R. I., & Head, J. D. 2011, *Phys. Chem. Chem. Phys.*, **13**, 11083
 Keane, J. V., Tielens, A. G. G. M., Boogert, A. C. A., Schutte, W. A., & Whittet, D. C. B. 2001, *A&A*, **376**, 254
 Kim, Y. S., & Kaiser, R. I. 2011, *ApJ*, **729**, 68
 Knez, C., Boogert, A. C. A., Pontoppidan, K. M., et al. 2005, *ApJ*, **635**, L145
 Kvenvolden, K., Lawless, J., Pering, K., et al. 1970, *Nature*, **228**, 923
 Lavalley, J., & Sheppard, N. 1972, *Spectrochim. Acta Part A Mol. Spectr.*, **28**, 2091
 Le Roy, L., Altwegg, K., Balsiger, H., et al. 2015, *A&A*, **583**, A1
 Leung, C. M., Herbst, E., & Huebner, W. F. 1984, *ApJS*, **56**, 231
 Linnartz, H., Ioppolo, S., & Fedoseev, G. 2015, *Int. Rev. Phys. Chem.*, **34**, 205
 Maeda, S., & Ohno, K. 2006, *ApJ*, **640**, 823
 Mahjoub, A., & Hodyss, R. 2018, *ApJ*, **869**, 98
 McClure, M. K., Boogert, A., Linnartz, H., et al. 2018, *AAS Meeting Abs.*, **232**, 302
 McGuire, B. A., Carroll, P. B., Dollhopf, N. M., et al. 2015, *ApJ*, **812**, 76
 Moore, M. H., Ferrante, R., Hudson, R., & Stone, J. 2007, *Icarus*, **190**, 260
 Mumma, M. J., & Charnley, S. B. 2011, *ARA&A*, **49**, 471
 Noble, J., Theule, P., Duvernay, F., et al. 2014, *Phys. Chem. Chem. Phys.*, **16**, 23604

- Oba, Y., Chigai, T., Osamura, Y., Watanabe, N., & Kouchi, A. 2014, *Meteorit. Planet. Sci.*, **49**, 117
- Öberg, K. I., Boogert, A. C. A., Pontoppidan, K. M., et al. 2008, *ApJ*, **678**, 1032
- Öberg, K. I., Boogert, A. C. A., Pontoppidan, K. M., et al. 2011, *ApJ*, **740**, 109
- Ogura, K., Migita, C. T., & Yamada, T. 1988, *Chem. Lett.*, **17**, 1563
- Ogura, K., Migita, C., & Yamada, T. 1989, *J. Photochem. Photobiol. A Chem.*, **49**, 53
- Ohishi, M., Suzuki, T., Hirota, T., Saito, M., & Kaifu, N. 2019, *PASJ*, **71**, 86
- Qasim, D., Fedoseev, G., Chuang, K.-J., et al. 2020, *Nat. Astron.*, **4**, 781
- Rachid, M. G., Terwisscha van Scheltinga, J., Koletzki, D., & Linnartz, H. 2020, *A&A*, **639**, A4
- Raunier, S., Chiavassa, T., Duvernay, F., et al. 2004, *A&A*, **416**, 165
- Romanescu, C., Marschall, J., Kim, D., Khatiwada, A., & Kalogerakis, K. S. 2010, *Icarus*, **205**, 695
- Schutte, W., & Khanna, R. 2003, *A&A*, **398**, 1049
- Schutte, W. A., Tielens, A. G. G. M., Whittet, D. C. B., et al. 1996, *A&A*, **315**, L333
- Soifer, B. T., Puetter, R. C., Russell, R. W., et al. 1979, *ApJ*, **232**, L53
- Suzuki, T., Ohishi, M., Hirota, T., et al. 2016, *ApJ*, **825**, 79
- Tempelmeyer, K., & Mills Jr. D. 1968, *J. Appl. Phys.*, **39**, 2968
- Terwisscha van Scheltinga, J., Ligterink, N. F. W., Boogert, A. C. A., van Dishoeck, E. F., & Linnartz, H. 2018, *A&A*, **611**, A35
- Theulé, P., Borget, F., Mispelaer, F., et al. 2011, *A&A*, **534**, A64
- Tielens, A. G. G. M., Allamandola, L. J., Bregman, J., et al. 1984, *ApJ*, **287**, 697
- Vinogradoff, V., Duvernay, F., Danger, G., et al. 2013, *A&A*, **549**, A40
- Wolff, H. 1970, *J. Chem. Phys.*, **52**, 2800
- Yamada, H., & Person, W. B. 1964, *J. Chem. Phys.*, **41**, 2478

Appendix A

This section presents the infrared spectra of pure and mixed methylamine ices. The spectra are focused on selected bands: the CH_3 antisymmetric stretch band around 2881.3 cm^{-1} ($3.471\text{ }\mu\text{m}$), the CH_3 symmetric stretch band around 2791.9 cm^{-1} ($3.582\text{ }\mu\text{m}$), the CH_3 antisymmetric deformation bands, at 1455.0 and

1478.6 cm^{-1} ($6.873\text{ }\mu\text{m}$ and $6.761\text{ }\mu\text{m}$), the CH_3 symmetric deformation band at 1420.3 cm^{-1} ($7.042\text{ }\mu\text{m}$), and the CH_3 rock at 1159.2 cm^{-1} ($8.621\text{ }\mu\text{m}$). Graphs displaying the peak position vs. FWHM for the bands and the relative band strengths are displayed at the bottom of each figure. The FWHM and peak position values displayed in the graphs are available from the Tables in Appendix B.

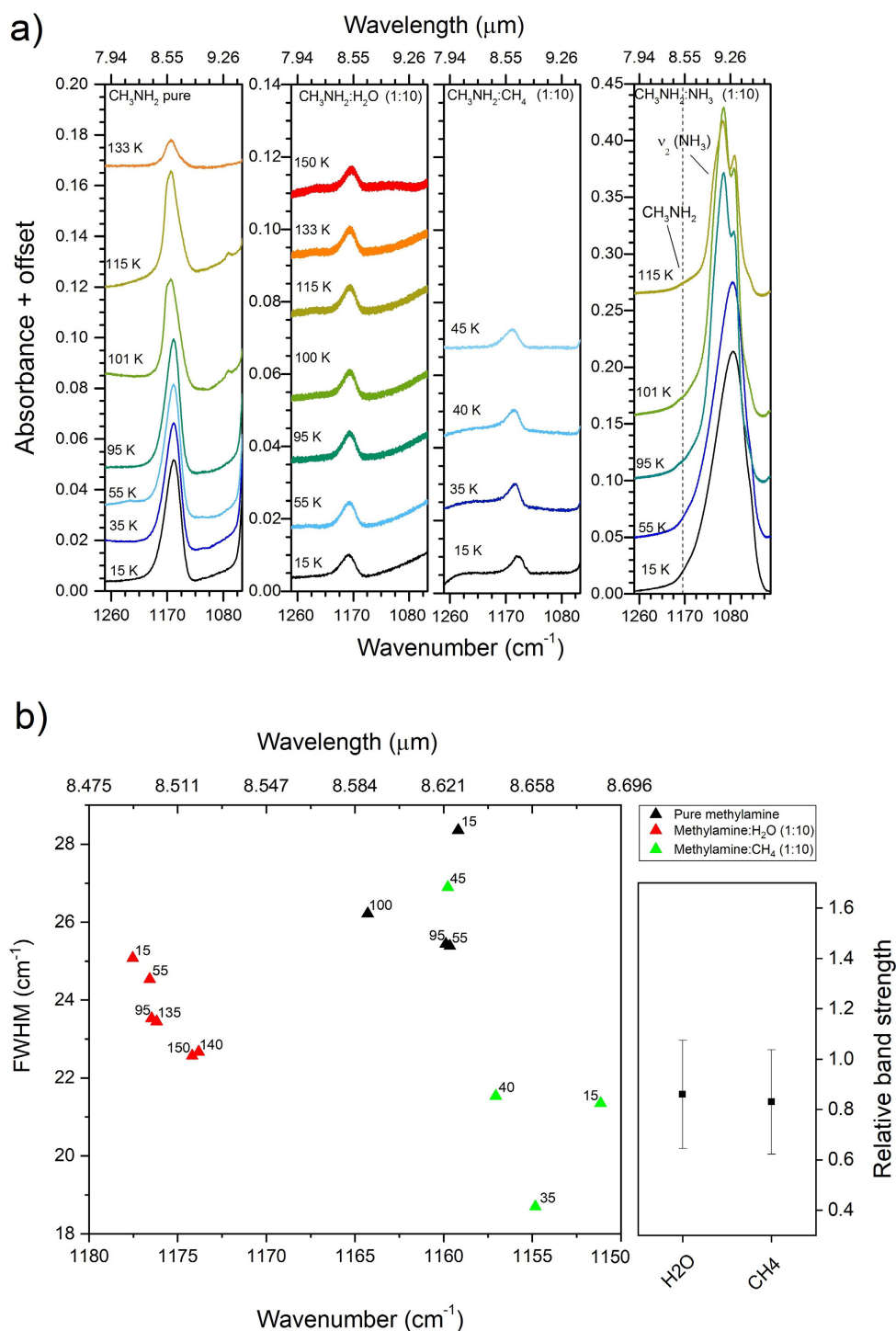


Fig. A.1. (a) Infrared band profile of the CH_3 rock vibrational mode of CH_3NH_2 , around 1159 cm^{-1} , in different ices at different temperatures, from left to right: pure CH_3NH_2 , $\text{CH}_3\text{NH}_2:\text{H}_2\text{O}$ (1:10), $\text{CH}_3\text{NH}_2:\text{CH}_4$ (1:10), and $\text{CH}_3\text{NH}_2:\text{NH}_3$ (1:10). The first and the last panels are displayed at a different Y-scale. In the last panel the CH_3NH_2 feature (whose position is indicated by the dashed line) appears as a shoulder in the ammonia ν_2 band (umbrella mode). (b) Left panel: peak position vs. FWHM for the CH_3 rock band in the ice mixtures displayed in a. Different mixtures are indicated by different colors, and the different temperatures are marked in the graph. Right panel: relative band strength of the CH_3 rock vibrational mode in different ice mixtures at 15 K.

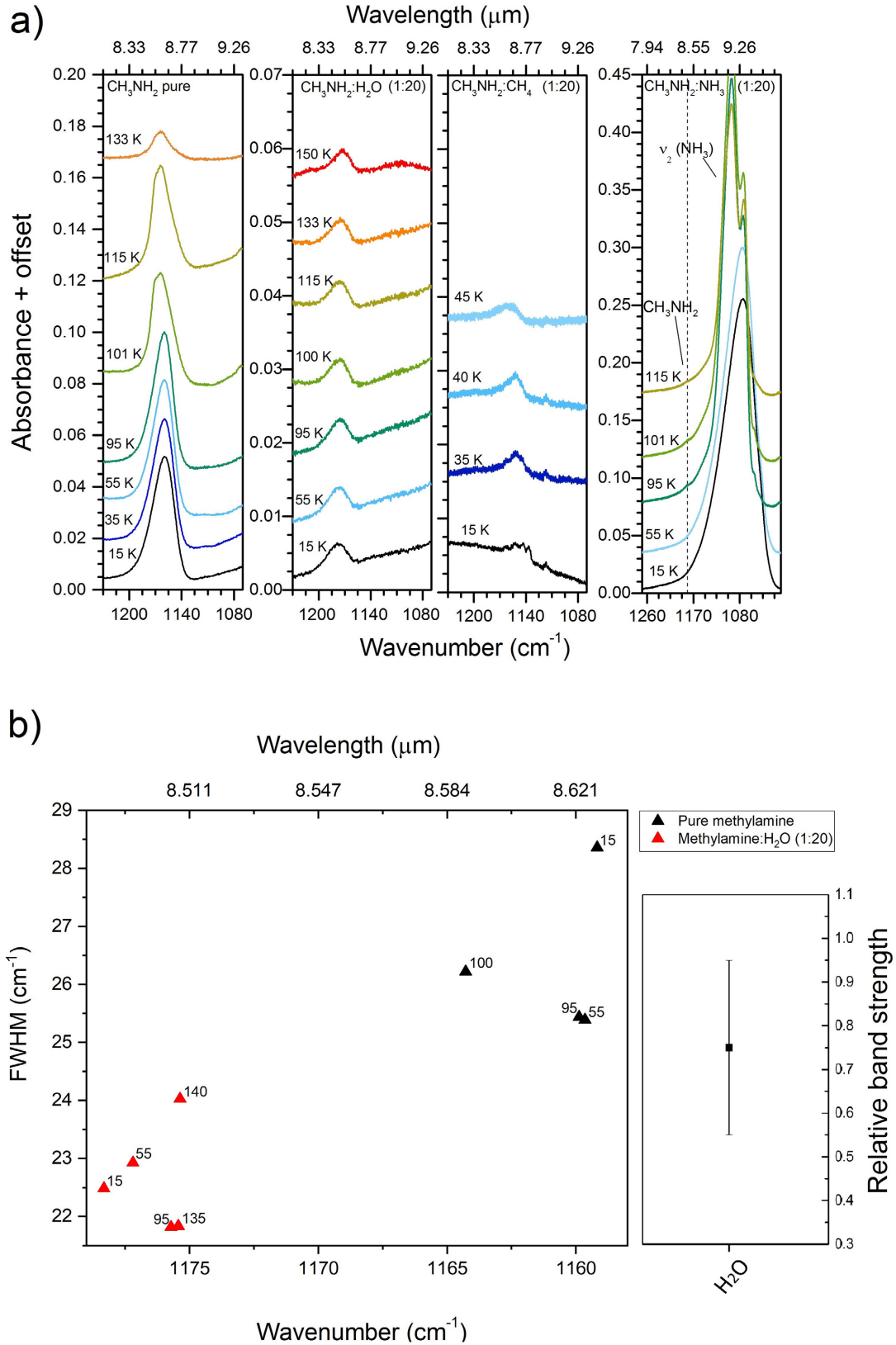


Fig. A.2. (a) Infrared band profile of the CH₃ rock vibrational mode of CH₃NH₂, around 1159 cm⁻¹, in different ices at different temperatures, from left to right: pure CH₃NH₂, CH₃NH₂:H₂O (1:20), CH₃NH₂:CH₄ (1:20), and CH₃NH₂:NH₃ (1:20). The first and the last panels are displayed at a different Y-scale. In the last panel the CH₃NH₂ feature (whose position is indicated by the dashed line) appears as a shoulder in the ammonia ν_2 band (umbrella mode). (b) *Left panel*: peak position vs. FWHM for the CH₃ rock band in the ice mixtures displayed in a. Different mixtures are indicated by different color and the different temperatures are marked in the graph. *Right panel*: relative band strength of the CH₃ rock vibrational mode at 15 K.

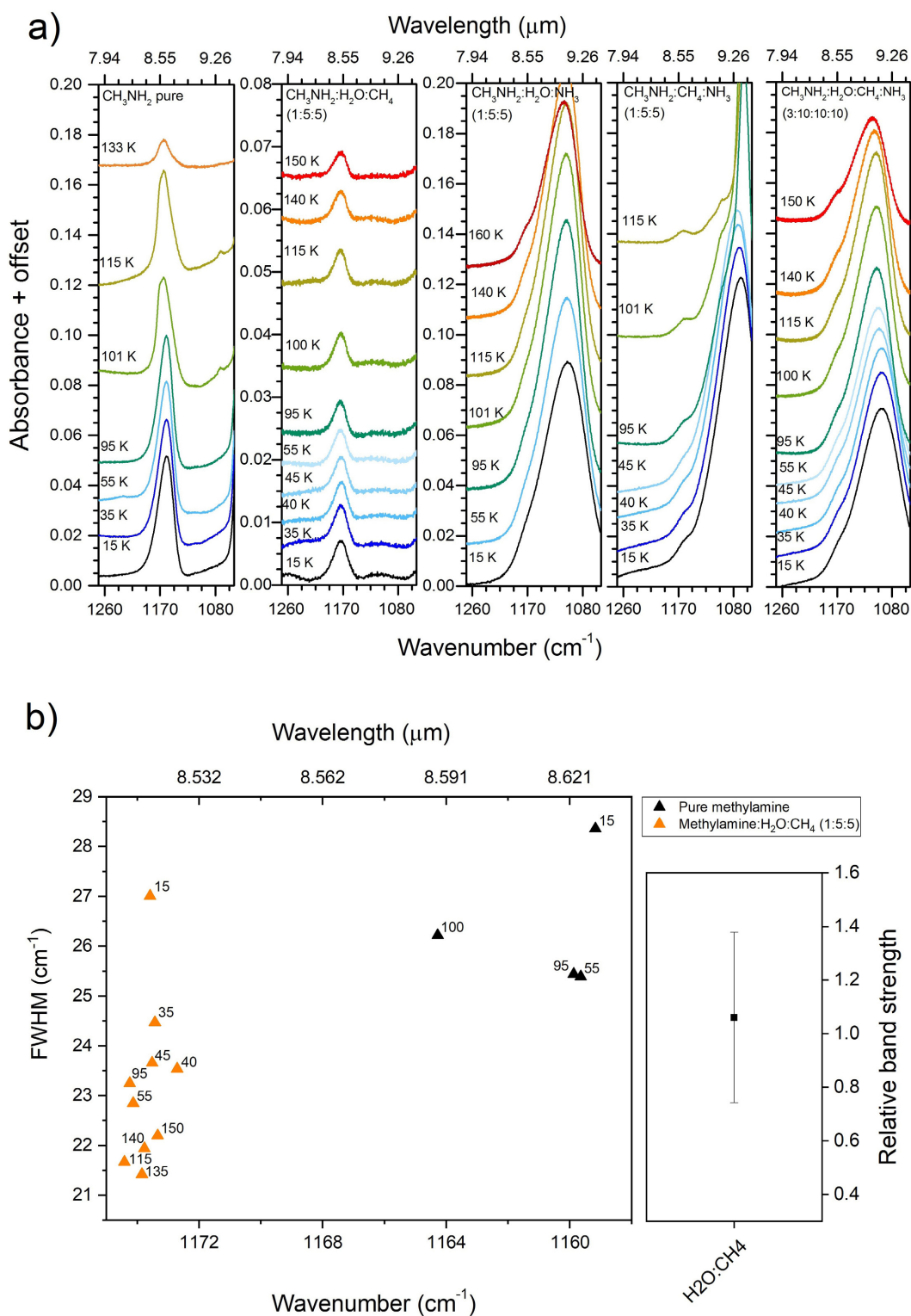


Fig. A.3. (a) Infrared band profile of the CH₃ rock vibrational mode of CH₃NH₂, around 1159 cm⁻¹, in different ices at different temperatures, from left to right: pure CH₃NH₂, CH₃NH₂:H₂O:CH₄ (1:5:5), CH₃NH₂:H₂O:NH₃ (1:5:5), CH₃NH₂:CH₄:NH₃ (1:5:5), and CH₃NH₂:H₂O:CH₄:NH₃ (3:10:10:10). The panels are displayed at a different Y-scale. In the last three panels, the CH₃NH₂ feature appears as a shoulder in the ammonia ν₂ band (umbrella mode). (b) *Left panel*: peak position vs. FWHM for the CH₃ rock band in the ice mixtures displayed in a. Different mixtures are indicated by different colors, and the different temperatures are marked in the graph. *Right panel*: relative band strength of the CH₃ rock vibrational mode at 15 K.

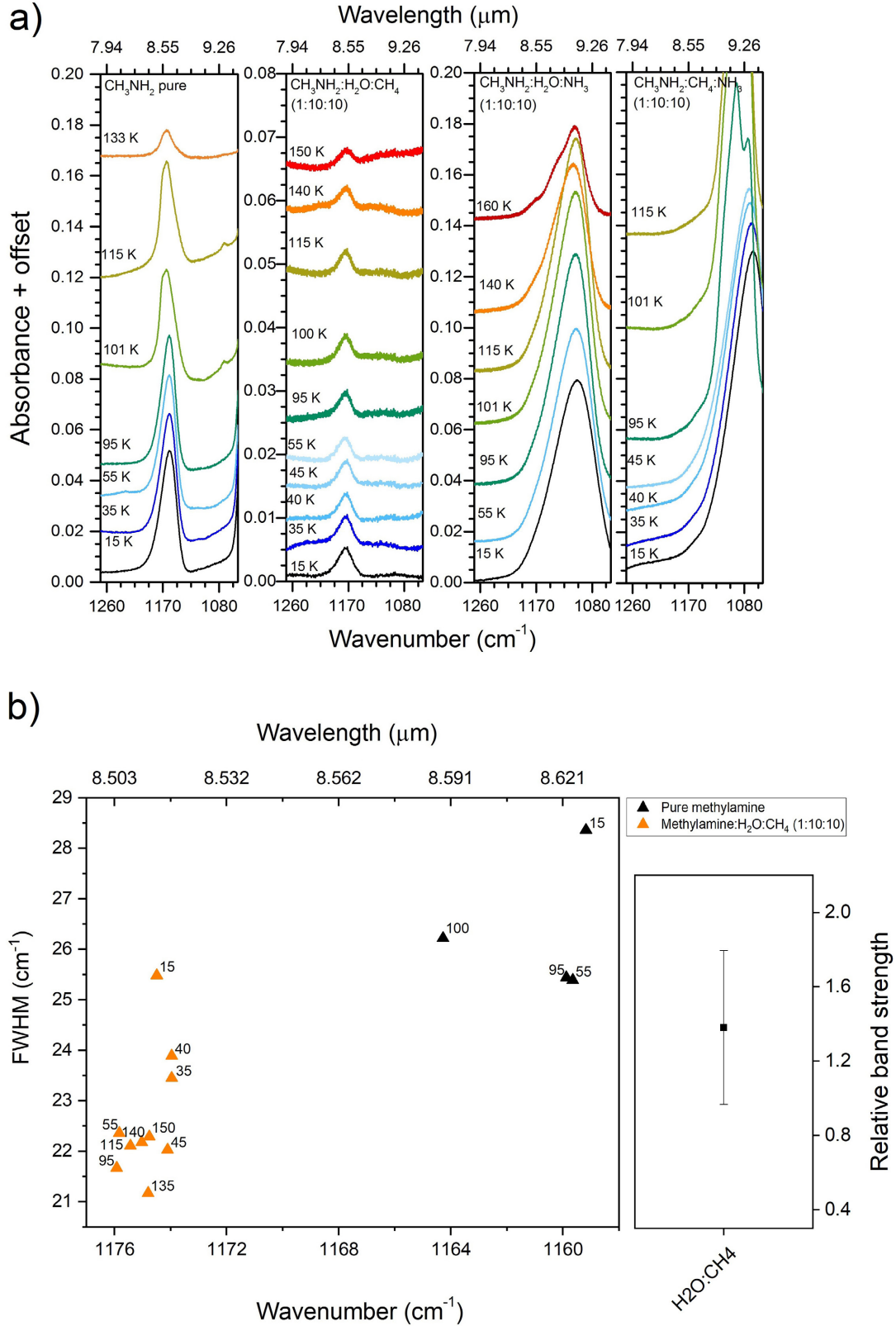


Fig. A.4. (a) Infrared band profile of the CH₃ rock vibrational mode of CH₃NH₂, around 1159 cm⁻¹, in different ices at different temperatures, from *left to right*: pure CH₃NH₂, CH₃NH₂:H₂O:CH₄ (1:10:10), and CH₃NH₂:H₂O:NH₃ (1:10:10). The last three panels are displayed at a different scale because the CH₃NH₂ feature appears as a shoulder in the band of the ammonia ν₂ mode (umbrella). (b) *Left panel*: peak position vs. FWHM for the CH₃ rock band in the ice mixtures displayed in a. Different mixtures are indicated by different colors, and the different temperatures are marked in the graph. *Right panel*: relative band strength of the CH₃ rock vibrational mode at 15 K.

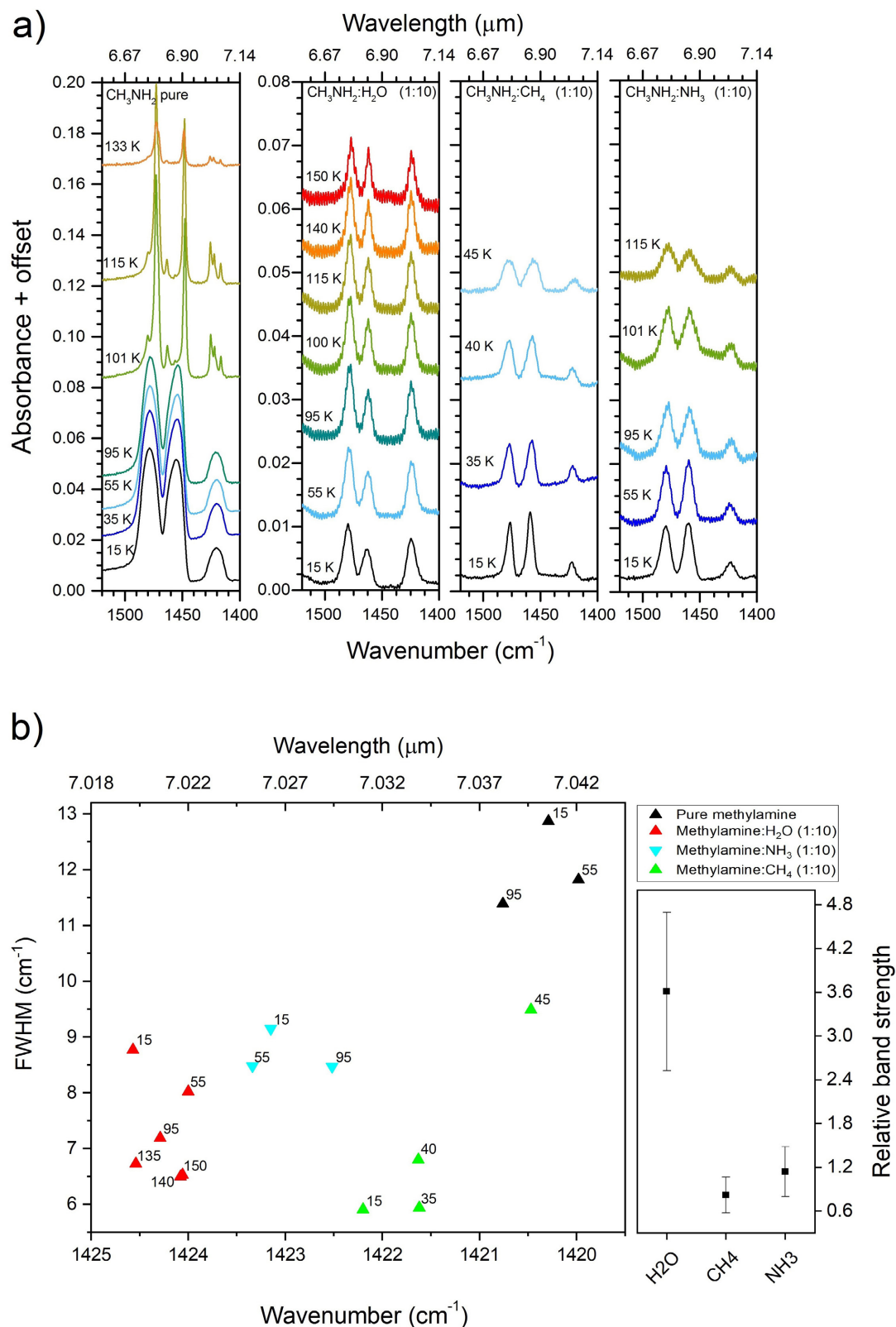


Fig. A.5. (a) Infrared band profile of the CH₃ antisymmetric deformation mode of CH₃NH₂ (the peaks around 1479 cm⁻¹ and 1455 cm⁻¹) and the CH₃ symmetric deformation mode (around 1420 cm⁻¹), in different ices at different temperatures, from *left to right*: pure CH₃NH₂, CH₃NH₂:H₂O (1:10), CH₃NH₂:CH₄ (1:10), and CH₃NH₂:NH₃ (1:10). (b) *Left panel*: peak position vs. FWHM for the CH₃ symmetric deformation band in the ice mixtures displayed in a. Different mixtures are indicated by different colors, and the different temperatures are marked in the graph. *Right panel*: relative band strength of the CH₃ symmetric deformation band (1420 cm⁻¹) in different ice mixtures at 15 K. *Panels c and d*: same as b for the CH₃ antisymmetric deformation modes, ν_5 and ν_{12} , at 1455 and 1478.6 cm⁻¹, respectively.

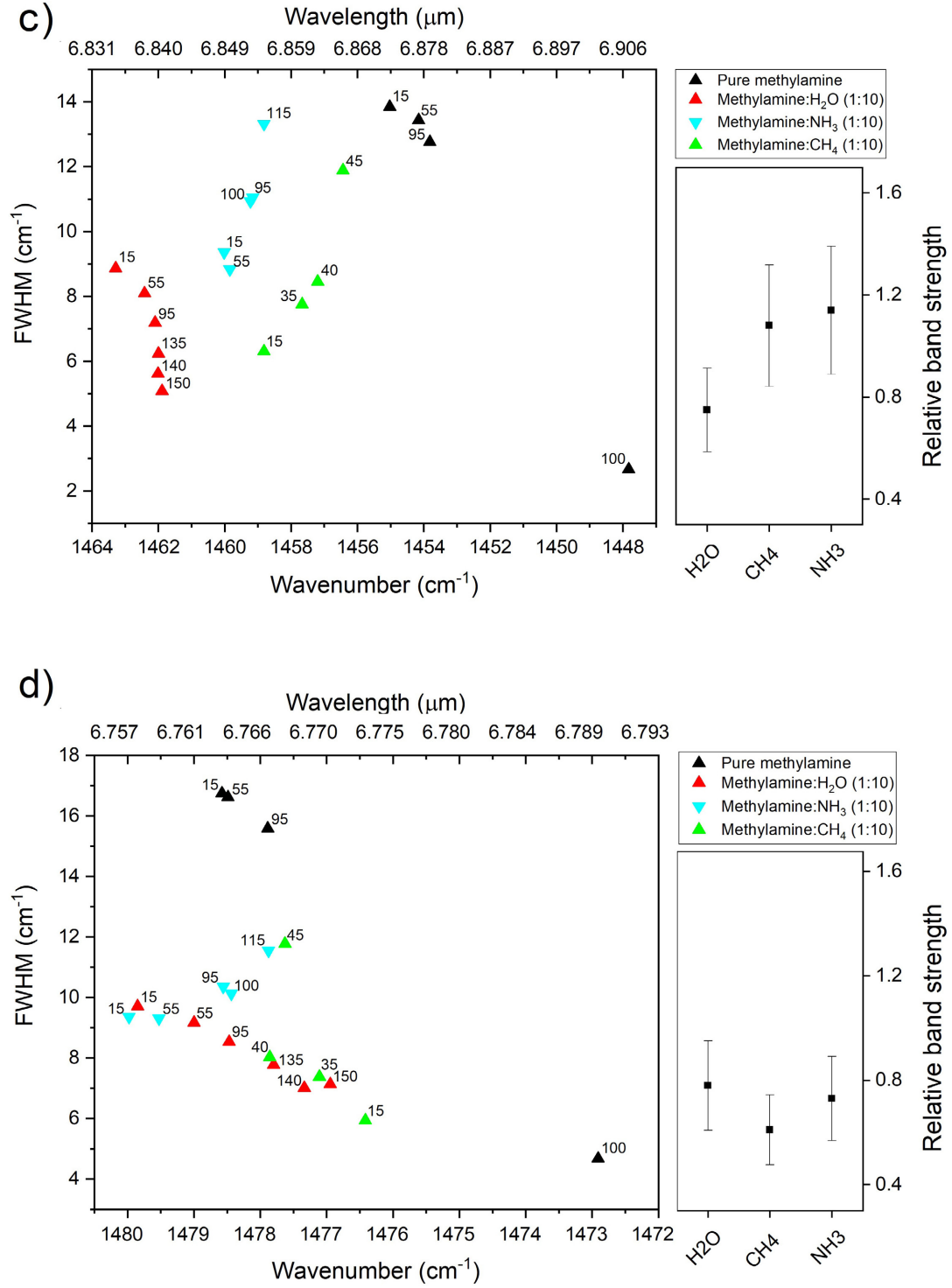


Fig. A.5. continued.

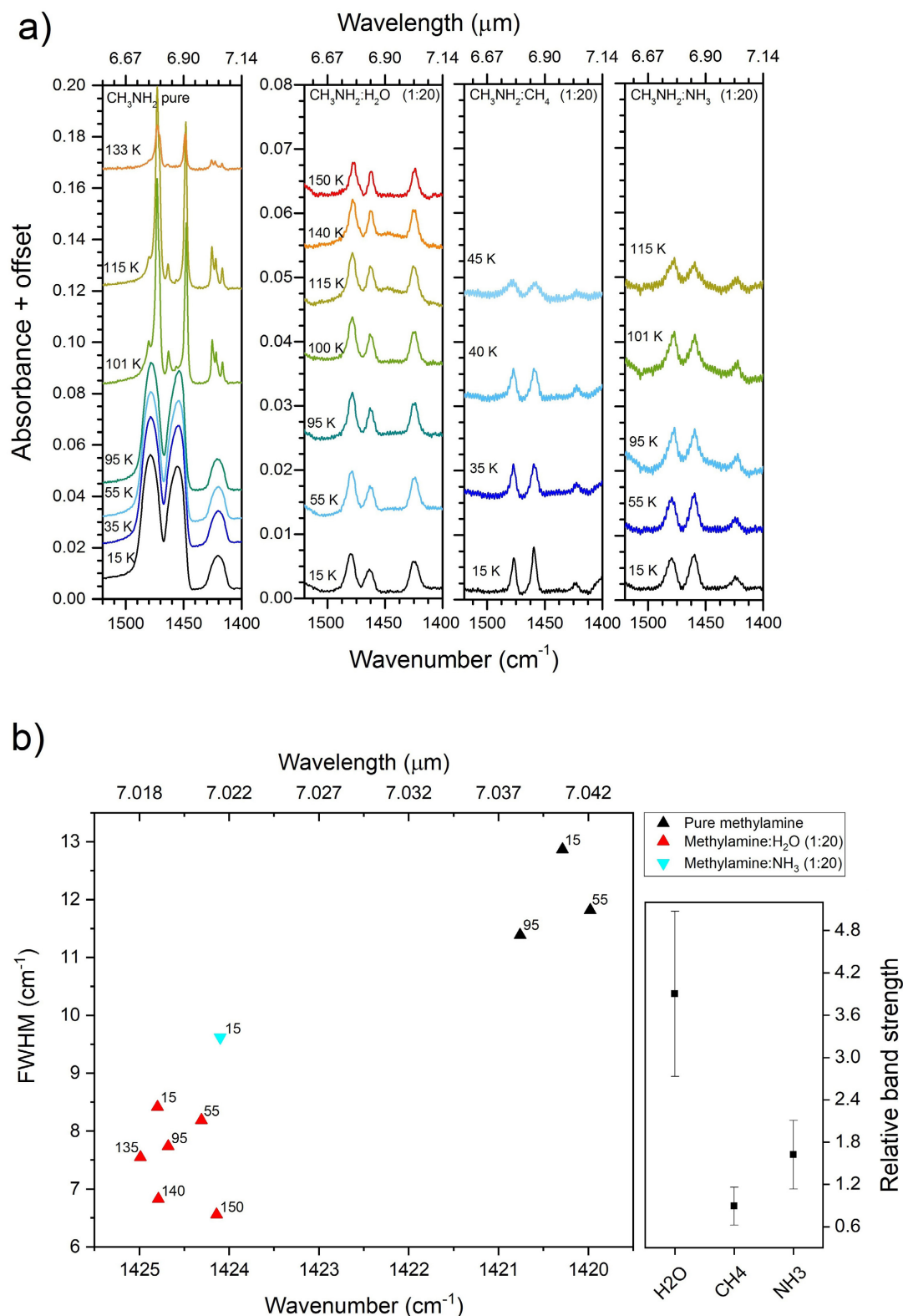


Fig. A.6. (a) Infrared band profile of the CH₃ antisymmetric deformation mode of CH₃NH₂ (the peaks around 1479 cm⁻¹ and 1455 cm⁻¹) and the CH₃ symmetric deformation mode (around 1420 cm⁻¹), in different ices at different temperatures, from *left to right*: pure CH₃NH₂, CH₃NH₂:H₂O (1:20), CH₃NH₂:CH₄ (1:20), and CH₃NH₂:NH₃ (1:20). (b) *Left panel*: peak position vs. FWHM for the CH₃ symmetric deformation band in the ice mixtures displayed in a. Different mixtures are indicated by different colors, and the different temperatures are marked in the graph. *Right panel*: relative band strength of the CH₃ symmetric deformation band (1420 cm⁻¹) in different ice mixtures at 15 K. *Panels c and d*: same as b for the CH₃ antisymmetric deformation modes, ν_5 and ν_{12} , at 1455 and 1478.6 cm⁻¹, respectively.

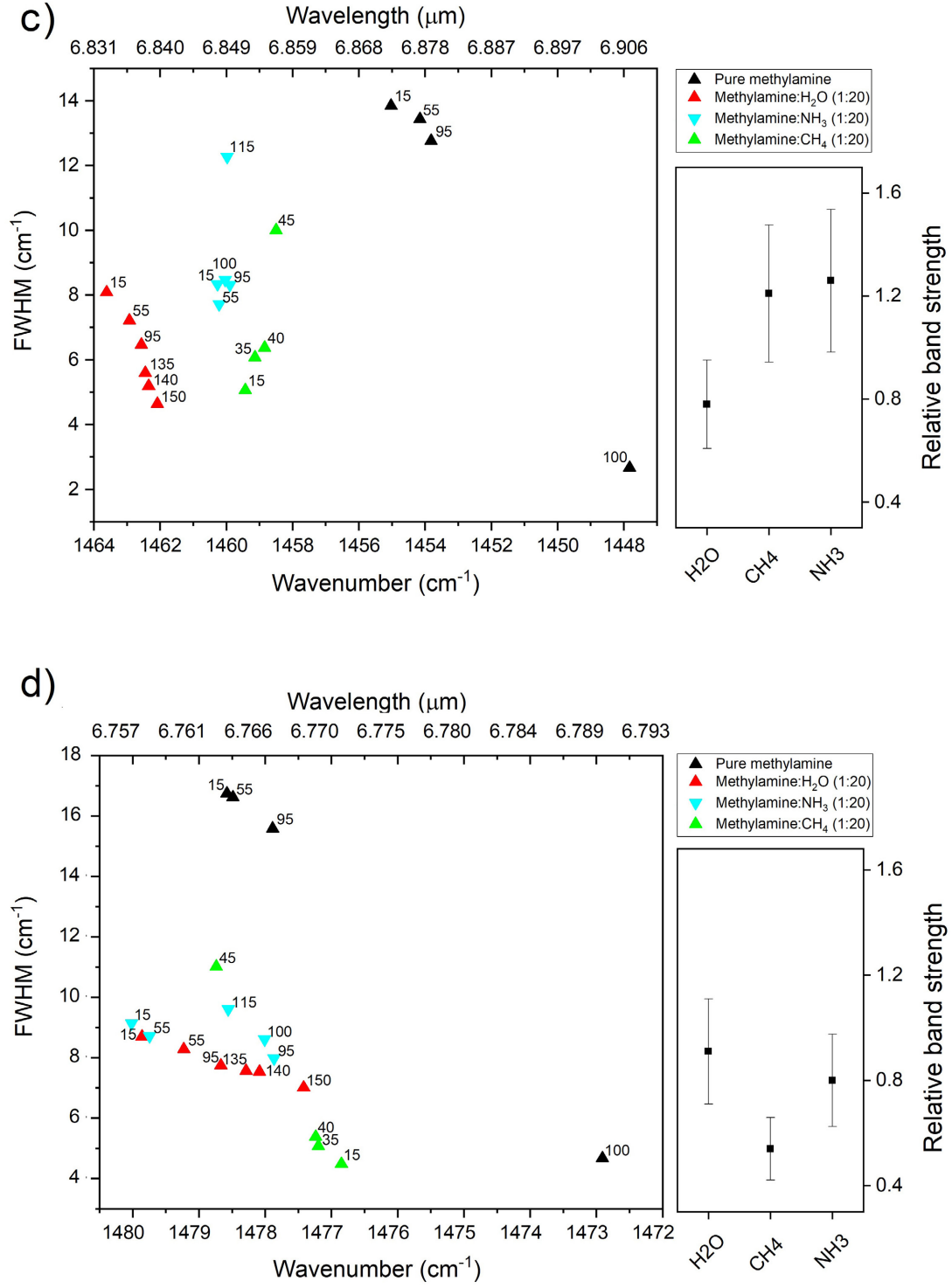


Fig. A.6. continued.

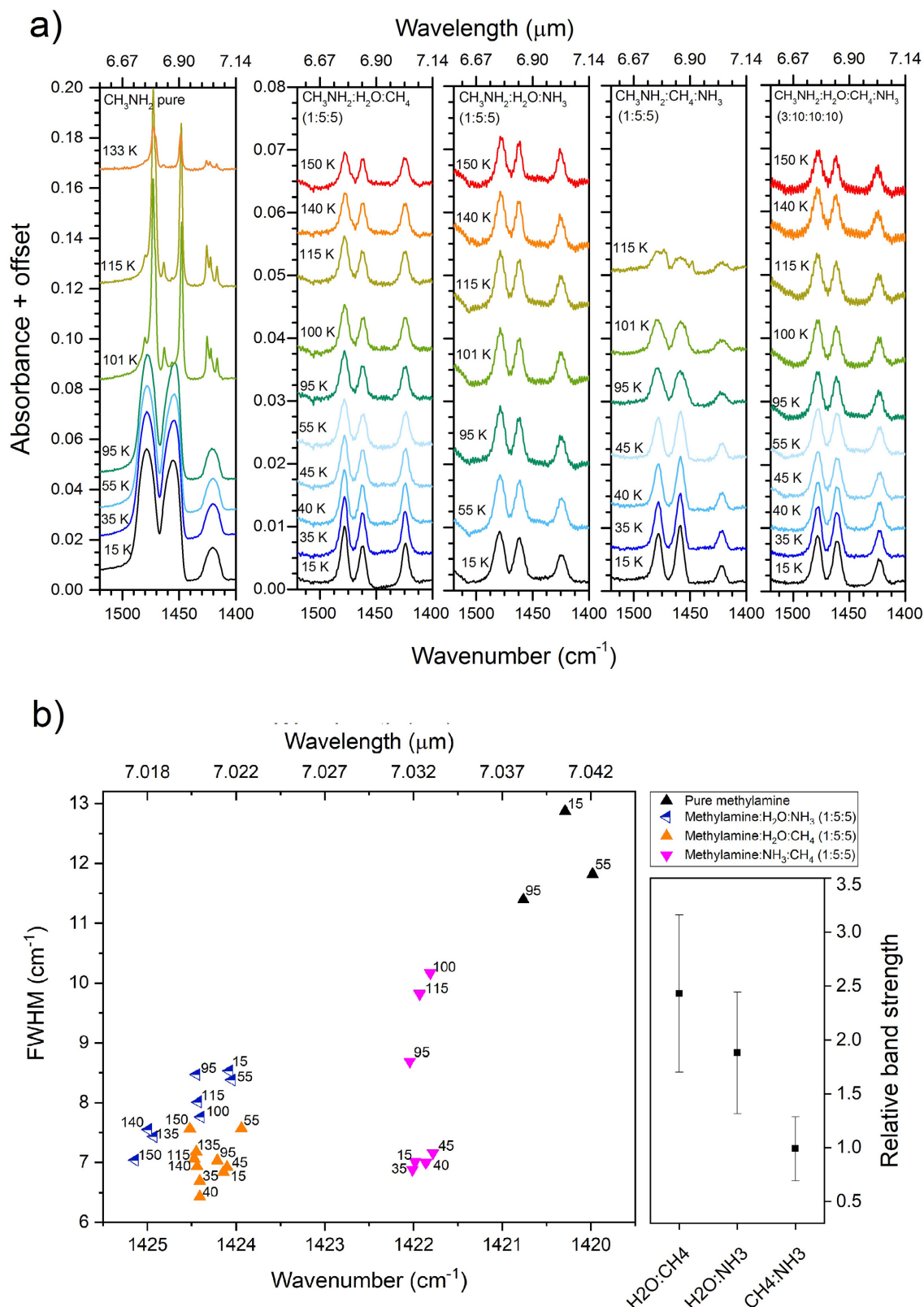


Fig. A.7. (a) Infrared band profile of the CH₃ antisymmetric deformation mode of CH₃NH₂ (the peaks around 1479 cm⁻¹ (ν_{12} mode) and 1455 cm⁻¹ (ν_5)) and the CH₃ symmetric deformation mode (around 1420 cm⁻¹), in different ices at different temperatures, from left to right: pure CH₃NH₂, CH₃NH₂:H₂O:CH₄ (1:5:5), CH₃NH₂:H₂O:NH₃ (1:5:5), CH₃NH₂:CH₄:NH₃ (1:5:5), and CH₃NH₂:H₂O:CH₄:NH₃ (3:10:10:10). (b) Left panel: peak position vs. FWHM for the CH₃ symmetric deformation band (1420 cm⁻¹) in the ice mixtures displayed in a. Different mixtures are indicated by different colors, and the different temperatures are marked in the graph. Right panel: relative band strength of the CH₃ symmetric deformation band in different ice mixtures at 15 K. Panels c and d: same as b for the CH₃ antisymmetric deformation modes, ν_5 and ν_{12} , at 1455 and 1478.6 cm⁻¹, respectively.

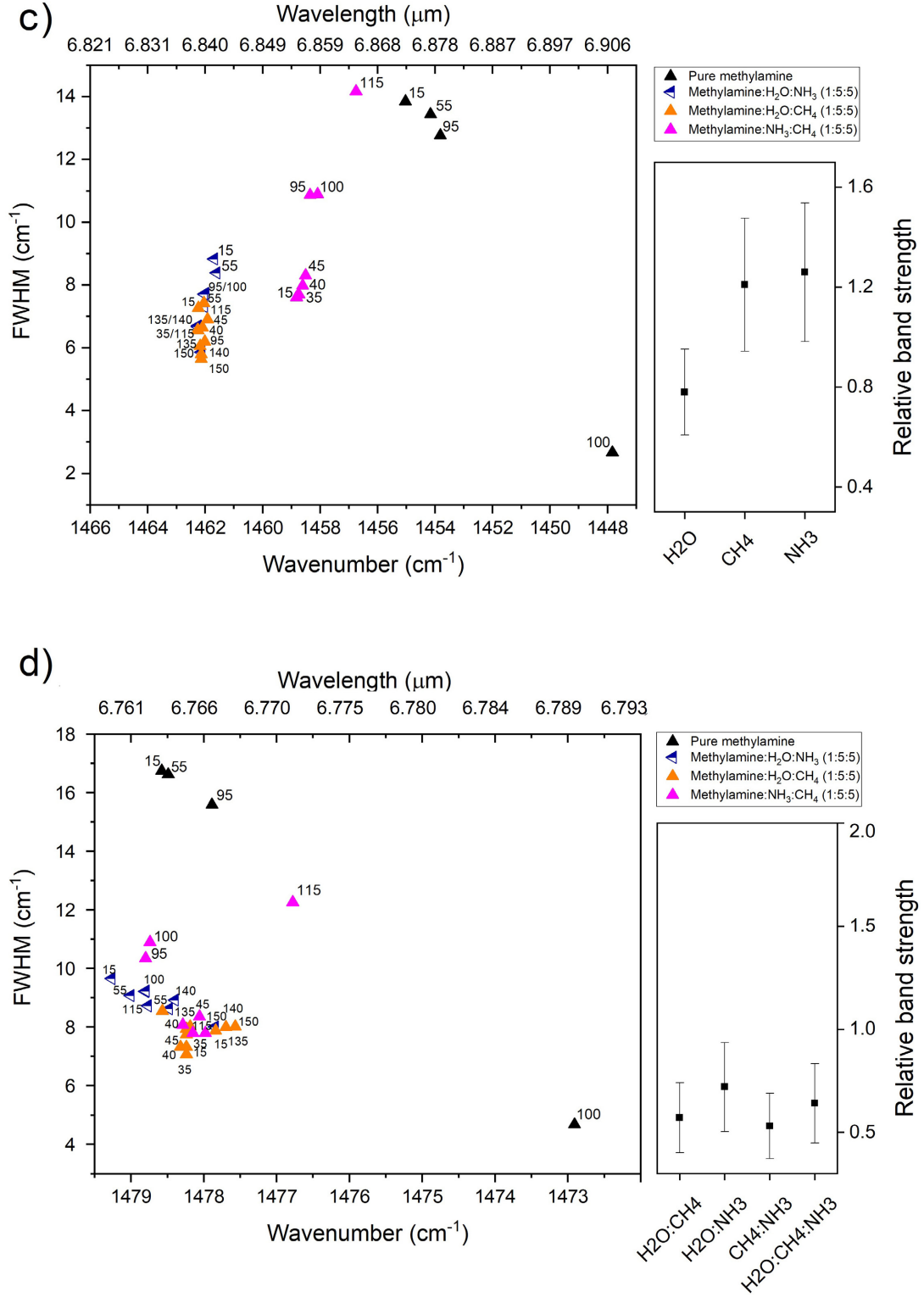
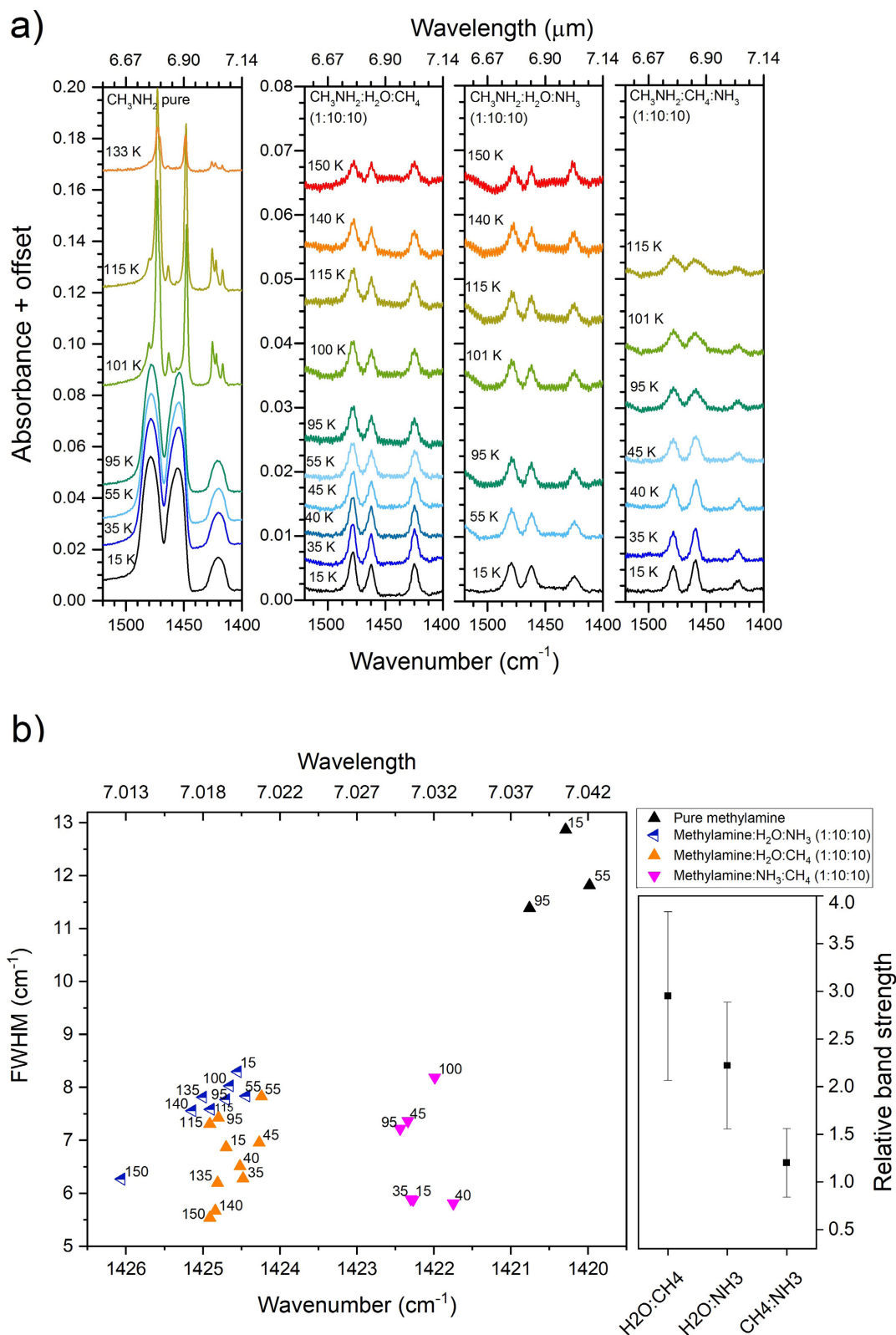


Fig. A.7. continued.



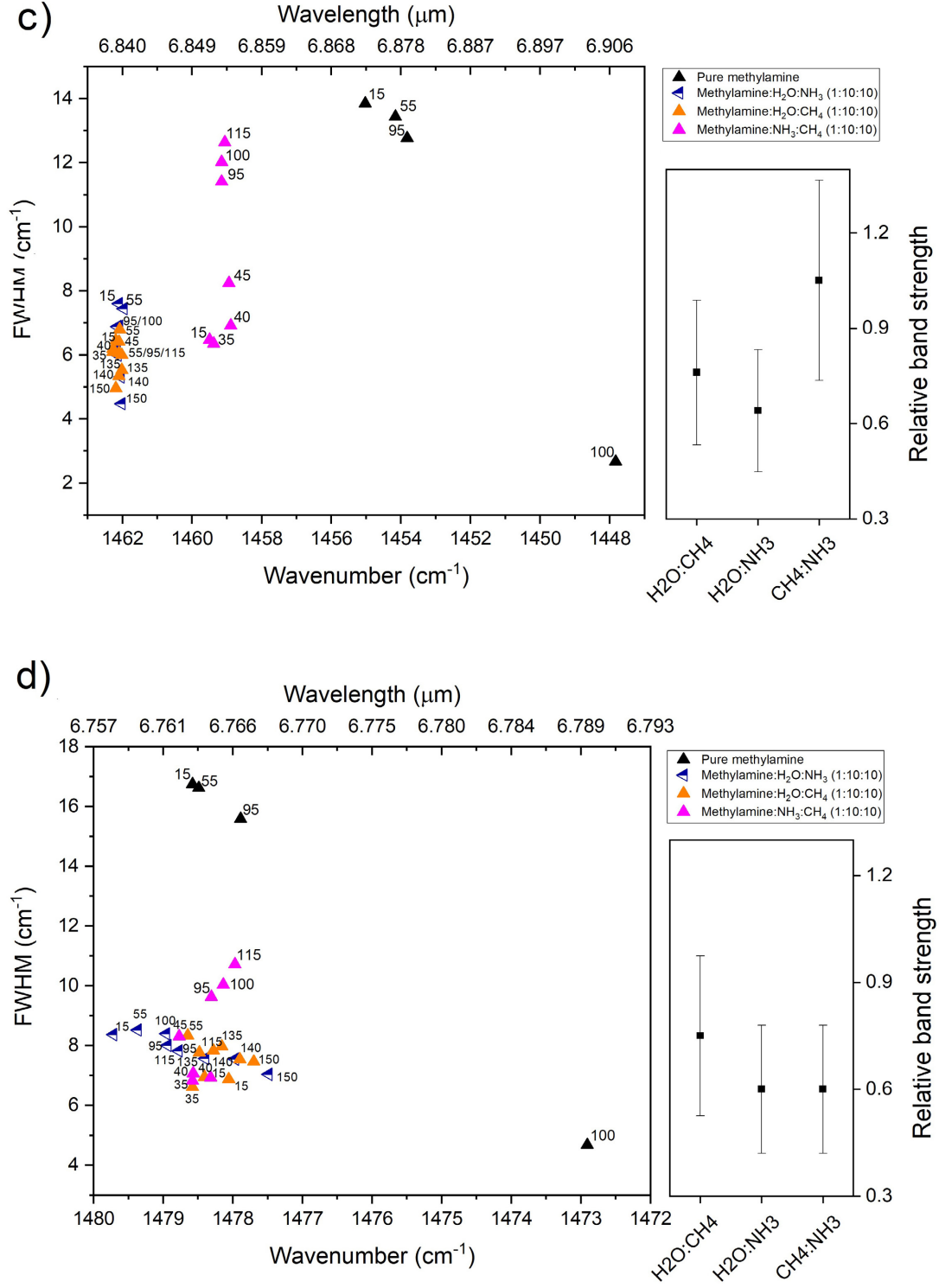


Fig. A.8. continued.

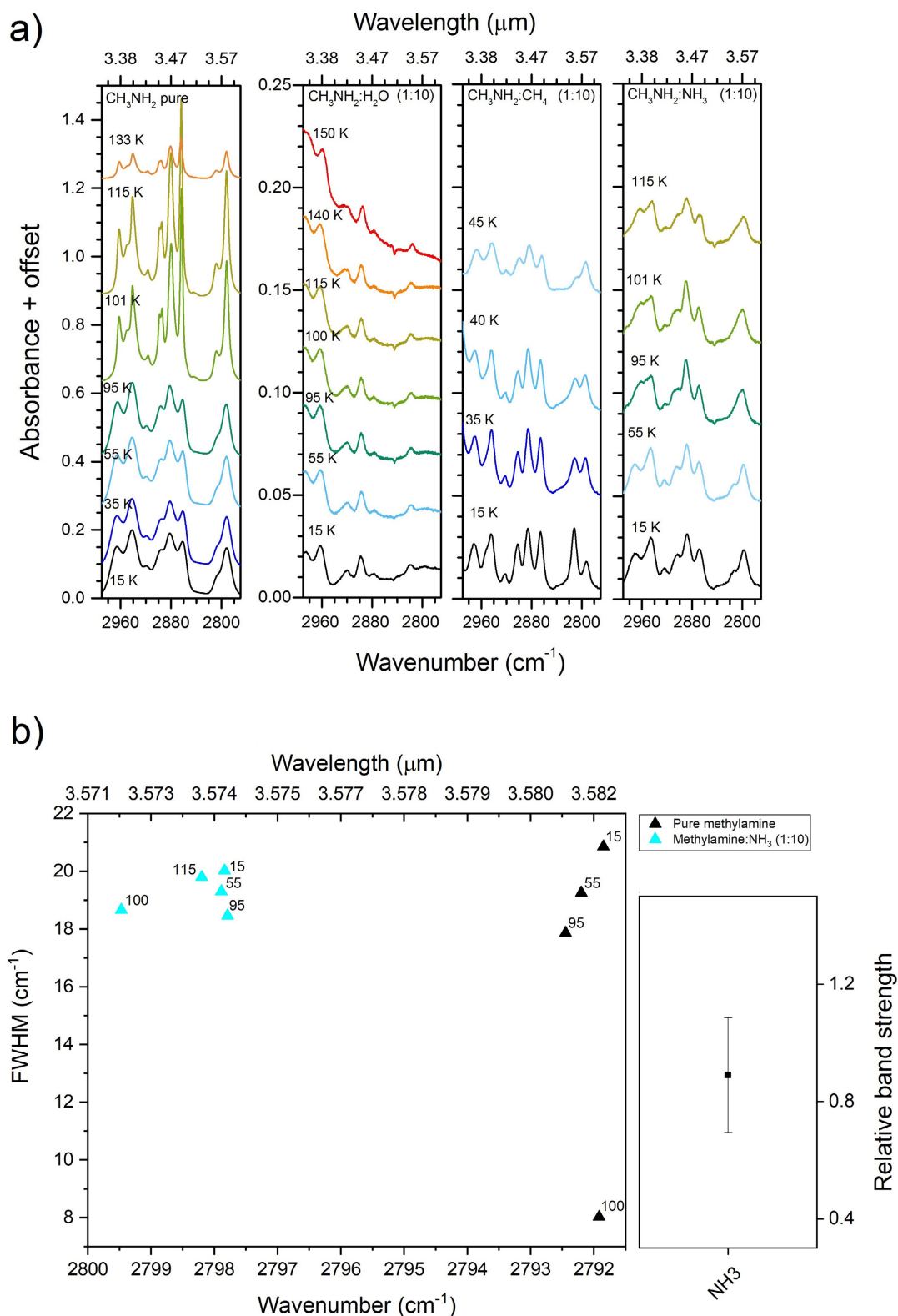


Fig. A.9. (a) 2750–3000 cm^{-1} region with spectra of different ices, from *left to right*: pure CH_3NH_2 , $\text{CH}_3\text{NH}_2:\text{H}_2\text{O}$ (1:10), $\text{CH}_3\text{NH}_2:\text{CH}_4$ (1:10), and $\text{CH}_3\text{NH}_2:\text{NH}_3$ (1:10). The CH_3 symmetric stretch mode of CH_3NH_2 (around 2792 cm^{-1}) lays in the rightmost region in all the panels. (b) *Left panel*: peak position vs. FWHM for the CH_3 symmetric stretch band in the ice mixtures displayed in a. Different mixtures are indicated by different colors, and the different temperatures are marked in the graph. *Right panel*: relative band strength of CH_3 antisymmetric stretch of $\text{CH}_3\text{NH}_2:\text{NH}_3$ (1:10) at 15 K. c same as b for the CH_3 antisymmetric stretch band (around 2881 cm^{-1}) in the ice mixtures displayed in a.

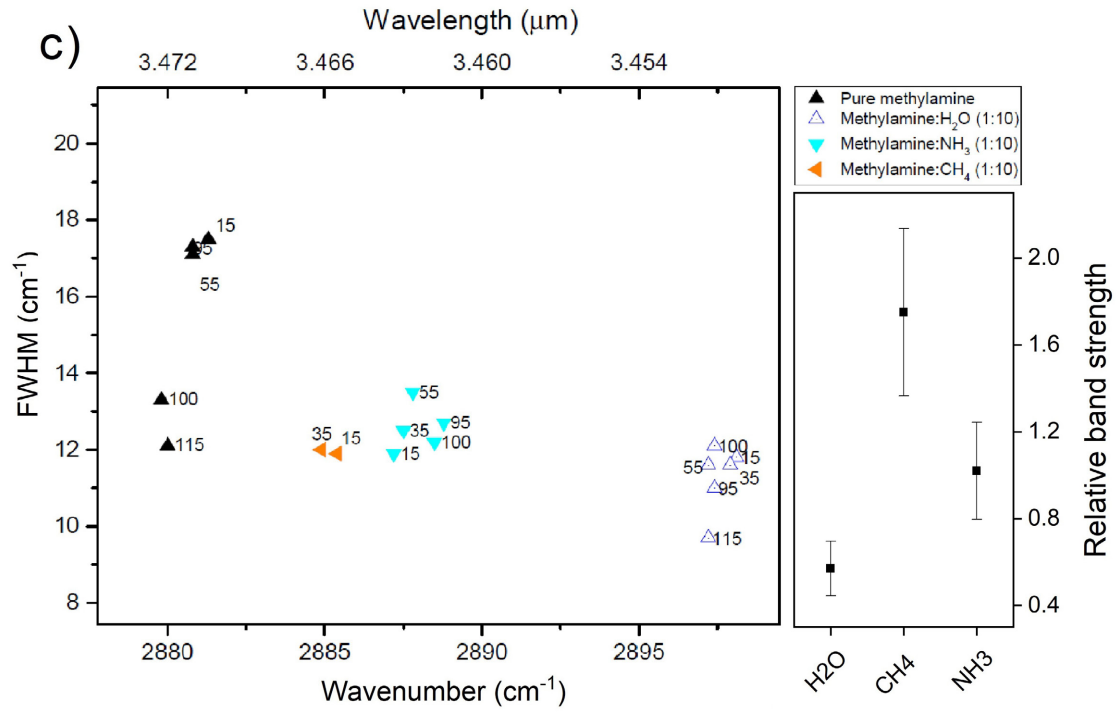


Fig. A.9. continued.

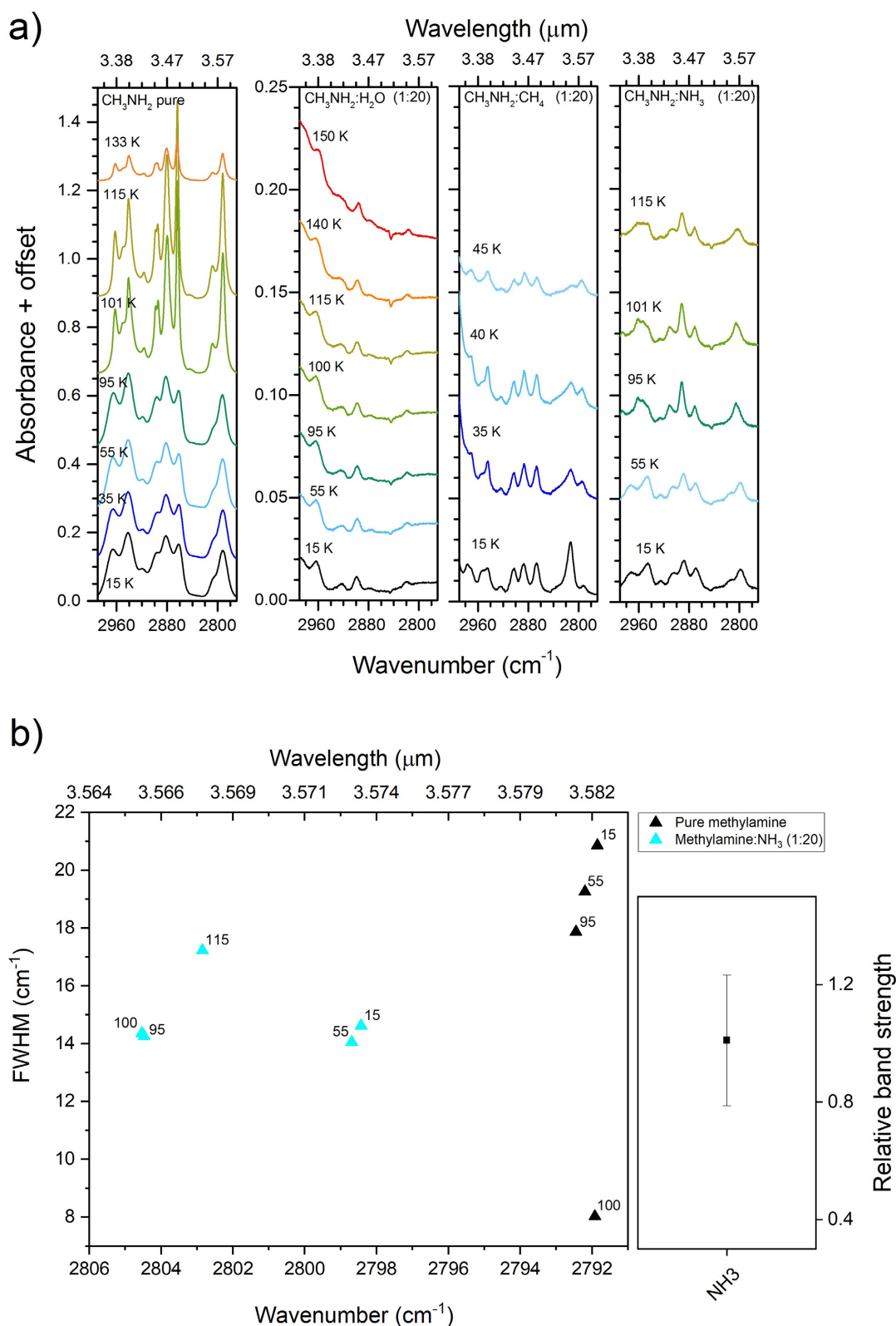


Fig. A.10. (a) 2750–3000 cm^{-1} region with spectra of different ices, from *left to right*: pure CH_3NH_2 , $\text{CH}_3\text{NH}_2:\text{H}_2\text{O}$ (1:20), $\text{CH}_3\text{NH}_2:\text{CH}_4$ (1:20), and $\text{CH}_3\text{NH}_2:\text{NH}_3$ (1:20). The CH_3 symmetric stretch mode of CH_3NH_2 (around 2792 cm^{-1}) lays in the rightmost region in all the panels. (b) *Left panel*: peak position vs. FWHM for the CH_3 symmetric stretch band in pure and $\text{CH}_3\text{NH}_2:\text{NH}_3$ (1:10) ices. *Right panel*: relative band strength of the CH_3 rock vibrational mode in different ice mixtures at 15 K. *c* same as *b* for the CH_3 antisymmetric stretch band (around 2881 cm^{-1}) in the ice mixtures displayed in *a*.

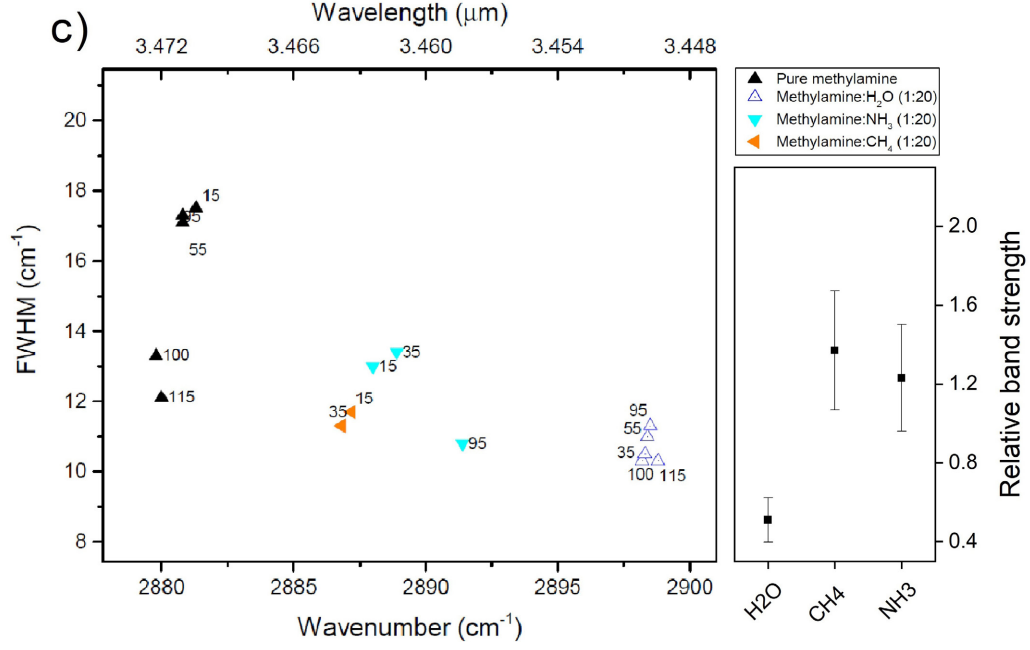


Fig. A.10. continued.

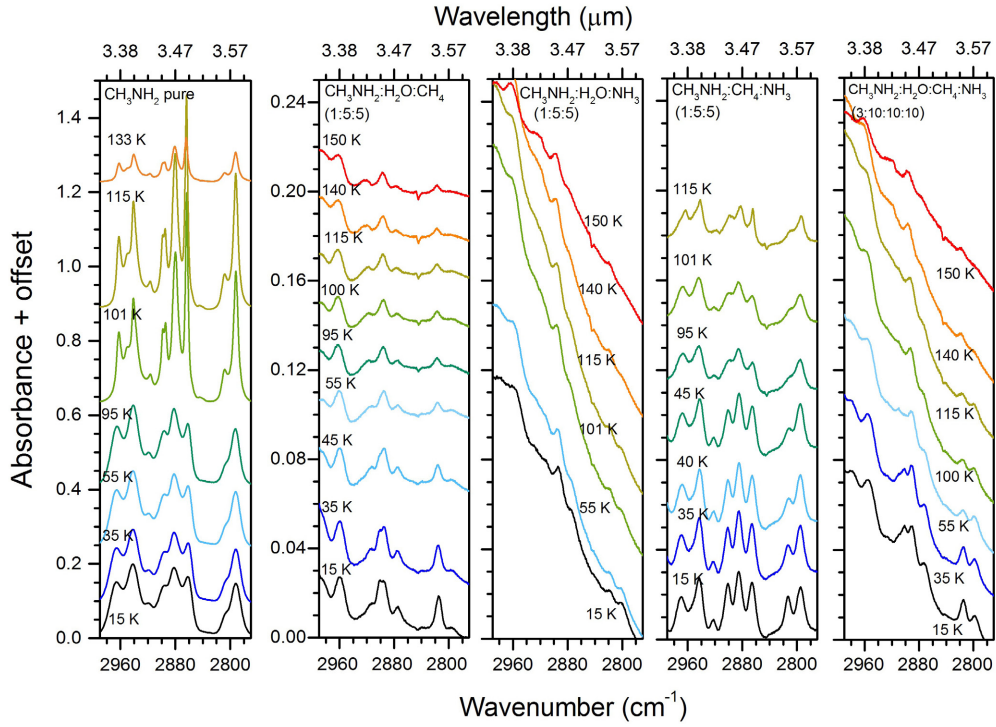


Fig. A.11. 2750–3000 cm⁻¹ region with spectra of different ices, from *left to right*: pure CH₃NH₂, CH₃NH₂:H₂O:CH₄ (1:5:5), CH₃NH₂:H₂O:NH₃ (1:5:5), CH₃NH₂:CH₄:NH₃ (1:5:5) and CH₃NH₂:H₂O:CH₄:NH₃ (3:10:10:10). The CH₃ antisymmetric stretch mode of CH₃NH₂ (around 2881 cm⁻¹) and the CH₃ symmetric stretch mode of CH₃NH₂ (around 2792 cm⁻¹) are displayed.

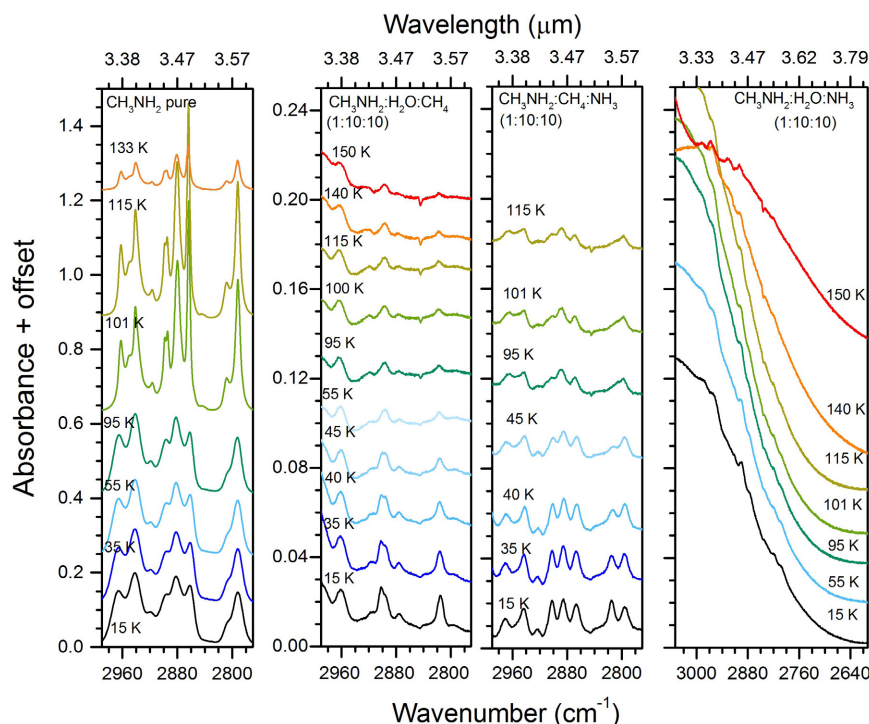


Fig. A.12. 2750–3000 cm^{-1} region with spectra of different ices, from left to right: pure CH_3NH_2 , $\text{CH}_3\text{NH}_2:\text{H}_2\text{O}:\text{CH}_4$ (1:10:10), $\text{CH}_3\text{NH}_2:\text{H}_2\text{O}:\text{NH}_3$ (1:10:10), and $\text{CH}_3\text{NH}_2:\text{CH}_4:\text{NH}_3$ (1:10:10). The CH_3 antisymmetric stretch mode of CH_3NH_2 (around 2881 cm^{-1}) and the CH_3 symmetric stretch mode of CH_3NH_2 (around 2792 cm^{-1}) are displayed.

Appendix B

Tables listing the peak positions and the FWHMs of the bands shown in Appendix A are available in electronic form at the CDS. Each table is composed of the measured peak position and FWHM for a given band in the mixtures with the same methylamine ratio and the pure ice for comparison. The peak position is measured for temperatures up to the desorption temperature of the methylamine ice matrix components (e.g., in the binary mixtures with CH_4 , the peak position and FWHM are calculated up to 55 K). The general uncertainty of peak positions is 0.5 cm^{-1} for all the measurements, and the typical error of the FWHM values amounts to a maximum of 1 cm^{-1} .

In the cases that the CH_3 antisymmetric deformation modes (around 1455 and 1479 cm^{-1}) overlap, the band profile is decomposed in two component features and the FWHM and peak position is calculated for each of the individual components.

The absorption profile between 2800 and 2900 cm^{-1} was decomposed into Gaussian features for the calculation of peak position and FWHM for the CH_3 antisymmetric stretch feature (2881.3 cm^{-1}).

In cases where the bands are weak or blended with matrix bands, the FWHM is not determined, and a rough peak position is given and marked with an asterisk (*). The resulting uncertainty is much larger than the peak positions that are derived for features that do not overlap.

Appendix C

The integrated absorbance of the methylamine bands (i.e., the band areas) in different ice mixtures and at selected temperatures is organized in tables available online at the CDS. Each table displays the data for one specific mixture. The band's integrated absorption is normalized in relation to the CH_3 antisymmetric deformation mode, around 1478.6 cm^{-1} , from the given mixture at 15 K. The CH_3 antisymmetric deformation mode was chosen for normalization because this feature is distinguishable in all the mixtures and does not overlap with any of the matrix components.